Word count: 13875

Revision 1

Coexisting hematite induces and accelerates the transformation of ferrihydrite: pathway and underlying mechanisms

Hongyan Wei [1,2,3], Jing Liu [4*], Qingze Chen [1,2,3], Yixuan Yang [1,2,3], Haiyang Xian [1,2,3], Xiaoliang Liang [1,2,3], Yiping Yang [1,2,3], Jianxi Zhu [1,2,3], Runliang Zhu [1,2,3*]

1. CAS Key Laboratory of Mineralogy and Metallogeny/Guangdong provincial Key Laboratory of Mineral Physics and Materials, Guangzhou Institute of Geochemistry, Chinese Academy of Sciences (CAS), Guangzhou, 510640 China

2. CAS Center for Excellence in Deep Earth Science, Guangzhou 510640, China

3. University of Chinese Academy of Science, Beijing, 100049 China

4. State Key Laboratory of Lunar and Planetary Sciences, Macau University of Science and Technology, Taipa 999078, Macau, China

*Corresponding author

E-mail: jingliu@must.edu.mo (Jing Liu); zhurl@gig.ac.cn (Runliang Zhu)

ABSTRACT

Crystallization induced by heterogeneous surfaces is an important process in geochemistry, biomineralization, and material synthesis, but the effects of heterogeneous surfaces on the transformation of metastable phases into new crystals remain poorly understood. In this work, we studied the transformation behaviors of ferrihydrite (Fhy) in the presence of hematite (Hem) nanoplates with specific exposed facets ({001} and {113}) at different pH (4, 7, and 12). Our results reveal that the Hem nanoplates can induce the transformation of Fhy to Hem/Gth (goethite) and accelerate the transformation rate. This effect is primarily achieved by modulating the dissolution-recrystallization process, i.e., accelerating the dissolution of Fhy and promoting the heterogeneous crystallization (to form new Hem/Gth) at the surface of added Hem nanoplates, and solution pH plays crucial roles in these processes. In specific, a relatively low supply of dissolved Fe^{3+} from Fhy at pH 4 favors island growth of new Hem at the {001} facets of Hem nanoplates and layer-by-layer growth at the {113} facets, which eventually results in the formation of thermodynamically stable pseudo-cubic morphology (exposing {012} facets). Because of the very low solubility of Fhy at pH 7, the induced transformation of Fhy by Hem nanoplates is rather weak. While at pH 12, a high supply of dissolved Fe^{3+} from Fhy benefits the layer-by-layer growth at {001} facets of Hem and the significant heteroepitaxial growth of Gth at the {113} facets. Besides the induced transformation, the direct solid-state transformation of Fhy into Hem and the homogeneous crystallization of dissolved Fe^{3+} also contribute to the transformation of Fhy. This study, for the first time, well reveals the mechanisms of induced transformation of Fhy in the presence of Hem nanoparticles, which will advance our understanding of the significant effects of heterogeneous surfaces in modulating the transformation of metastable phases, and supplement the transformation mechanisms of Fhy.

Keywords: Iron oxides; Crystallization; Phase transformation; Heterogeneous surfaces;

43 Facet-specific

INTRODUCTION

Crystallization is a critical process in geochemistry, biomineralization, and materials synthesis and a comprehensive understanding of the crystallization mechanism is of great importance (Thanh et al., 2014; De Yoreo et al. 2015; Gilbert et al. 2019; Fu et al. 2022). Crystallization involves both classical and non-classical pathways. The former is based on the monomer-by-monomer addition of simple chemical species (i.e., atoms, ions, and molecules) from solutions (Kulmala 2003; Habraken et al. 2013; Jun et al., 2022); while the latter is thought to involve intermediate metastable stages (e.g., prenucleation clusters, amorphous phases, metastable phases) preceding the formation of a thermodynamically stable phase, and the crystal can grow through the attachment of preformed metastable intermediate particles (Yuwono et al. 2010; Gebauer et al. 2014; Jehannin et al. 2019). Previous studies have shown that pH, temperature, coexisting ions, heterogeneous surfaces, etc., can affect both the classical and nonclassical crystallization pathways (Jung and Jun, 2016; Riechers et al. 2017, 2022; Jiang et al. 2018a). Among these factors, the heterogeneous surfaces provided by coexisting solids can significantly affect the crystallization process through a distinctive surface-induced manner, which has gained considerable attentions in the past decades (Riechers et al. 2017; Li and Deepak 2022; Molnár et al. 2023; Yang et al. 2023).

Heterogeneous surfaces-controlled nucleation and growth of crystals are widespread in the nature (particularly in soils and sediments), and have been quite often applied for synthesizing composite functional materials (Putnis 2014; Jung et al. 2016; Molnár et al. 2023). For example, mineral surface-induced oxidation and crystallization of Mn(II) is a vital pathway for the abiotic formation of manganese oxide minerals in the nature, which is crucial to the widespread formation of rock varnish (Hu et al. 2023; Yang et al. 2023); macromolecules-directed nucleation and growth of nanocrystals are important steps in building vertebrate skeletal systems and other rigid biological structures in biological systems

(Addadi et al. 2003; Nudelman et al. 2010); surface-induced growth of nanoparticles is an important method in regulating the morphology and function of nanomaterials (Duan et al. 2012; Huang et al. 2014). Numerous studies have revealed that heterogeneous surfaces can affect the nucleation and growth of ions from solutions at/near the surfaces through reducing the free energy barrier, increasing solute concentration, serving as nucleation templates, etc., which then can always accelerate the crystallization processes and even alter the crystallization pathway (Li et al. 2014; Thanh et al. 2014; Zhu et al. 2021; Liu et al. 2021a).

Despite that the significant influence of heterogeneous surfaces on the formation of crystals has been well recognized, a large knowledge gap still remains in this field. Until now, most studies focused on the effects of heterogeneous surfaces on the crystallization behaviors of solution ions (Jun et al. 2010, 2016; Xu et al. 2014a; Liu et al. 2021a), but their effects on the transformation of poor crystalline or metastable phases to stable minerals have been overlooked. Indeed, Earth is a nonequilibrium system wherein the reactions are simultaneously controlled by both dynamic and thermodynamic factors, and thus the reaction products are always trapped at local, instead of global, energy minimum position in the energy landscape, forming a diversity of metastable products (Hochella et al. 2008, 2019). For example, the secondary minerals formed in the complex supergene environment always have metastable structures, and thus metastable minerals are ubiquitous in the nature and coexist with other solid matters (Politi et al. 2008; Rodriguez-Navarro et al. 2016; Jiang et al. 2018a). In this term, the effects of heterogeneous surfaces on the transformation of metastable phases should play a crucial role in controlling the formation of secondary minerals and the geochemical cycle of elements in Earth's surface environments.

Ferrihydrite (Fhy) is the first formed mineral during the quick hydrolysis of Fe^{3+}, and it is a typical metastable iron (oxyhydr)oxide mineral. Fhy can easily transform to other stable iron oxides, e.g., to goethite (Gth) through dissolution-recrystallization pathway and to

hematite (Hem) through direct solid-phase transformation (Michel et al. 2007; Das et al. 2011a, b; Zhu et al. 2016). The transformation rates and pathways of Fhy can be affected by various factors, e.g., pH, temperature, and coexisting substances, which have been the subject of extensive studies (Das et al. 2011a, b; ThomasArrigo et al. 2020; Namayandeh et al., 2022; Wei et al. 2023). For example, recent studies have shown that the surface of clay minerals can strongly interact with Fhy particles to reduce the aggregation of Fhy particles, and thus hinder their transformation (Yan et al. 2021; Wei et al. 2023). Notini et al. (2022) discovered that the surface of Gth can facilitate the Fe^{2+}-catalyzed transformation of Fhy to Gth via template-directed nucleation and growth. Despite that these recent limited studies have unveiled the complex effects of heterogeneous surfaces on the transformation of Fhy, the underlying mechanisms remain largely unknown, with the atomic/nano-scale information at mineral surfaces being particularly scarce.

Hem is a naturally abundant and thermodynamically the most stable iron oxide, and it can form through the solid-state transformation of Fhy or direct nucleation from the solution and can be preserved over long geological periods (Cornell and Schwertmann 2003; Hoashi et al. 2009). As such, the preexisting Hem could coexist with Fhy in the nature, and thus possess effects on the transformation behaviors of Fhy. As we know, the surfaces of mineral particles are indeed composed of a collection of different facets, and the Hem particles exposing particular facets (e.g., {001}, {113}, and {012} facets) have been found in the nature (Huang et al. 2016; Yuan et al. 2017). Hem particles with specific crystal facets possess distinctive atomic structures and thus may exhibit quite different surface reactivities (e.g., adsorption, catalysis, and heterogeneous nucleation); and the related studies can well link macroscopic reaction properties to the atomic structure of Hem (Chan et al. 2015; Wu et al. 2018; Liu et al. 2021a). For example, Liu et al. (2021a) directly observed the facet-specific oxidation of Mn(II) and nucleation/growth of Mn oxides on different Hem facets, and

revealed the crystallographic relationship between Mn oxides and specific Hem facets (e.g., lattice matching between particular facets of the two minerals). In this term, Hem with specific exposed facets should be an ideal mineral for studying the effects of heterogeneous surfaces on the transformation behaviors of Fhy at the atomic/nano-scale, which, to the best of our knowledge, has not been concerned in previous studies.

The objective of this study is to investigate the effects of specific facets of Hem on the phase transformation of metastable Fhy, and further elucidate the significant roles of heterogeneous surfaces on the nucleation and growth of crystals. Hexagonal Hem nanoplates, exposing {001} and {113} facets, were utilized to provide well-defined heterogeneous surfaces. The mineral phases and their relative contents were characterized using X-ray powder diffraction (XRD) and room temperature ^{57}Fe Mössbauer spectroscopy (MS). The morphology and structure of these samples were analyzed via scanning electron microscopy (SEM) and transmission electron microscopy (TEM). This study may shed new light on the transformation of Fhy in the presence of Hem nanoplates, and the nanoscale details of the growth mechanisms of Hem nanoplates will be revealed as well. Our findings may not only provide new insights into the phase transformation behaviors of Fhy, but also advance our understanding of the significant effects of mineral surfaces on the transformation of metastable phases.

EXPERIMENTAL METHODS

Materials

Analytical-grade $Fe(NO_3)_3 \cdot 9H_2O$, $FeCl_3 \cdot 6H_2O$, ammonium oxalate, oxalic acid, NaOH, and HNO_3 were purchased from Aladdin Chemistry Co. Ltd or Macklin. Sodium acetate was of analytical degree and obtained from Richjoint. All of the chemicals were used without any additional treatments. All suspensions were prepared using ultrapure water (with a resistivity

143 of 18.2 MΩ·cm).

144 **Synthesis of Fhy nanoparticles and Hem nanoplates**

145 The synthesis of Fhy was carried out using a protocol based on previous studies,
146 involving the rapid hydrolysis of $Fe(NO_3)_3 \cdot 9H_2O$ (Cornell and Schwertmann 2003).
147 Specifically, a desired amount of 1 M $Fe(NO_3)_3 \cdot 9H_2O$ solution was titrated to pH 7-8 by 3 M
148 NaOH under continuous magnetic stirring. Subsequently, the suspension was allowed to
149 equilibrate for a period of approximately 2 h. All precipitates were washed four times with
150 ultrapure water by centrifugation at 11000 rpm for 10 min and then stored in the refrigerator
151 before use. The Hem nanoplates were synthesized according to Liu et al. (2021a). In brief,
152 3.28 g $FeCl_3 \cdot 6H_2O$ was dissolved in 120 ml ethanol with 8.4 ml ultrapure water, and then 9.6
153 g sodium acetate was added to the suspension. The suspension was stirred for 4 h at ambient
154 temperature, transferred to a Telon-lined stainless-steel autoclave (200 ml), and heated at
155 180°C in an oven for 18 h. The Hem precipitates were collected after cooling to room
156 temperature, and rinsed three times with water and ethanol, respectively. Finally, the collected
157 precipitates were freeze-dried, ground, and stored in a desiccator before use.

158 **The transformation of Fhy in the presence of Hem heterogeneous surfaces**

159 Hydrothermal experiments were conducted to investigate the impact of Hem surfaces on
160 the transformation of Fhy, and the transformation reaction with various solution pH and Hem
161 nanoplate contents were studied in detail. The transformation experiments were carried out in
162 sealed 250 ml polypropylene bottles at a temperature of 75°C in a water bath. These bottles
163 were labeled as Fhy-a or Fhy-*x*Hem-a, in which *x* and a denote the Hem nanoplate mass ratio
164 (i.e., Hem/(Hem+Fhy)) and pH value, respectively. To explore the effect of solution pH on
165 the Fhy transformation in the presence of Hem surfaces, a specific amount of Fhy precipitates
166 was resuspended in 600 ml ultrapure water to achieve 2.4 g Fhy (calculated based on the

167 $Fe(OH)_3$ formula) per 100 ml water. This suspension was then divided into six parts in
168 polypropylene bottles labeled as Fhy-4, Fhy-20Hem-4, Fhy-7, Fhy-20Hem-7, Fhy-12, and
169 Fhy-20Hem-12, respectively. For the three Fhy-20Hem suspensions, 0.6 g of Hem nanoplates
170 were added to obtain a Hem mass ratio of 20 wt%. The pH of these suspensions was adjusted
171 to the desired value (4, 7, or 12) and stirred for 2 h before initiating the transformation at
172 75°C. The pH was not readjusted during these reactions.

173 After hydrothermal reaction for 0, 1, 3, 5, 7, and 10 days at pH 4 and 7 or 0, 1, 2, 4, 8,
174 12, and 24 h at pH 12, 15 ml of the suspension was collected from the bottles to study the
175 kinetics of Fhy transformation. These collected suspensions were denoted as Fhy-a-b or Fhy-
176 *x*Hem-a-b, in which *x*, a, and b represent the mass ratio of Hem nanoplates, pH value, and
177 reaction time, respectively (e.g., Fhy-20Hem-4-10d denotes the sample with 20 wt% Hem
178 nanoplates reacted at pH 4 for 10 days). Finally, these suspensions were centrifuged at 11000
179 rpm for 10 min to remove the supernatant, and the resulting precipitates were freeze-dried for
180 further analysis. Different solution pH (4, 7, and 12) was applied in this work to illuminate
181 the specific mechanisms of Hem heterogeneous surfaces that affect the transformation of Fhy,
182 in which Fhy would mainly undergo dissolution-recrystallization to Gth at pH 4 and pH 12,
183 and aggregation-dehydration to Hem at pH 7 (Das et al. 2011a, b; Yan et al. 2020). The
184 temperature selected in this work was to accelerate the transformation of Fhy in a reasonable
185 time, which is widely applied in other studies and will not change the transformation
186 pathways and product types of Fhy (Das et al. 2011a, b; Zhang et al. 2018; Ye et al. 2021).

187 To investigate the effect of added Hem contents on the transformation of Fhy, a certain
188 amount of Fhy precipitates was resuspended in 300 ml ultrapure water to reach 2.4 g Fhy per
189 100 ml water. This suspension was then divided into six portions, ensuring that each portion
190 contained approximately 1.2 g of Fhy. Different amounts of Hem nanoplates were added to
191 these suspensions to achieve Hem/(Hem + Fhy) mass ratios of 0 wt%, 5 wt%, 10 wt%, 20

wt%, 40 wt%, and 70 wt%, respectively. These suspensions were denoted as Fhy, Fhy-5Hem, Fhy-10Hem, Fhy-20Hem, Fhy-40Hem, and Fhy-70Hem, respectively (these numbers represent the ratio of added Hem). These suspensions were adjusted to pH 4, which not only was close to the natural environments but also reflected the difference in the transformation behaviors of Fhy in different systems, as revealed in our preliminary experiments. These solutions were then stirred for 2 h before starting the transformation at 75°C. The suspensions were sampled after reacting for 0, 1, 3, and 10 days, and dealt with the same procedures above. It needs to be stated that the Fhy synthesized in different batches and the different volumes of reaction systems might slightly influence the final transformation results, especially the ratios of the products. Hence, the effect of Hem surfaces on the transformation of Fhy at different solution pH and added Hem contents is only compared in separate systems.

Characterization methods

The X-ray powder diffraction (XRD) data were collected on a Rigaku MiniFlex-600 X-ray diffractometer. The measurement was performed under the following conditions: Cu Kα radiation, 40 kV, 15 mA, 3-70° 2θ, 0.01° 2θ step, and 10° 2θ min^{-1}. XRD can offer semi-quantitative information about the phase contents, as the intensity of the diffraction peak is directly related to the content of the mineral phases. The relative content of Hem and Gth in the final products was determined using the *k*-value method (Text S1 and Table S1), employing RIR values of 3.26 and 2.79 for Hem and Gth, respectively (Gualtieri 2000). Room temperature ^{57}Fe Mössbauer spectroscopy (MS) operated in the transmission and constant acceleration mode utilizing a WSS-10 instrument with ^{57}Co as the radioactive source. The *MossWinn* program was used to determine the compositions and their relative contents. Furthermore, the degree of the transformation of Fhy in different samples was determined by selective dissolution experiments, in which Fhy was dissolved by 0.2 M ammonium oxalate at pH 3 under dark conditions (Lin et al. 2003; Yan et al. 2020). The Fe content of the

unreacted samples was denoted as Fe_o, and the Fe content of the reacted samples after different times was labeled as Fe_t. The ratios of Fe_t/Fe_o represent the residual content of Fhy after different times of transformation.

Scanning electron microscopy (SEM) images were acquired using a Carl Zeiss Supra 55 field emission scanning electron microscope. The samples before and after the transformation were mounted on conductive glue and then fixed on the holder for morphology observation. Transmission electron microscopy (TEM) and High-resolution transmission electron microscopy (HRTEM) were performed with an FEI Talos F200S TEM at an accelerating voltage of 200 kV. The samples were gently crushed to powder, dispersed in absolute alcohol, and sonicated before being deposited onto a holey copper film and dried in air. HRTEM is an effective tool to characterize the relationship between heterogeneous surfaces and newly formed minerals from the perspective of the crystal lattice.

RESULTS

Structural characterization of Fhy and Hem

The two broad reflections in the XRD pattern demonstrated that Fhy was poorly crystalline (the inset in Fig. S1a). Moreover, the SEM image showed that Fhy particles formed large aggregates (Fig. S1a), which was in agreement with the results from prior studies (Yan et al. 2020; Wei et al. 2023). The sharp reflections in the XRD pattern showed good crystallinity of Hem without other impurities (the inset in Fig. S1b). The morphology and structure of Hem were further characterized using SEM, TEM, and HRTEM, showing hexagonal nanoplates (Fig. S1b and c). The HRTEM images of a horizontally lying particle recorded the interplanar spacing of 0.25 nm with 60° intersection angles, corresponding to Hem (110), ($\bar{1}$20), and ($\bar{2}$10) planes (Fig. 1d). The corresponding fast Fourier transfer (FFT) pattern exhibited a set of diffraction spots possessing hexagonal symmetry, which can be

indexed as the [001] zone axis of Hem (the inset in Fig. S1d). This phenomenon implied that the nanoplates are single crystals and the bottom/top surface was bounded by {001} planes. Furthermore, the side facets were proved to be equivalent and belonged to {113} facets in previous studies (Chan et al. 2015; Liu et al. 2021a).

SEM was employed to analyze the samples containing mixed Fhy and Hem nanoplates before hydrothermal transformation (Fig. S2). For the Fhy-20Hem sample, the SEM images showed that Fhy was mainly reserved as large aggregates at pH 4 and 12 (Fig. S2a and c), whereas smaller aggregates were observed at pH 7 (Fig. S2b). Noticeably, the morphology of some Hem nanoplates changed slightly after stirring for 2 h at pH 12 (Fig. S2d), indicating that the added Hem nanoplates began to grow before hydrothermal treatment due to the quick dissolution of Fhy at pH 12. With respect to the samples containing different Hem contents, SEM results showed that the Fhy particles still existed as aggregates in the presence of 5 wt% and 70 wt% Hem nanoplates at pH 4 (Fig. S2e and f). These results suggested that the addition of Hem nanoplates under acidic and alkaline pH could not effectively disperse the Fhy aggregates. Previous studies have demonstrated that the pH_{zpc} of Fhy and Hem are ~7-8 (Chatman et al. 2013; Yan et al. 2021). As a result, the similar charge of Hem and Fhy under acidic and alkaline conditions led to the inefficient electrostatic attraction between the two minerals, subsequently impeding the dispersion of Fhy aggregates by Hem. However, since pH 7 is close to the pH_{zpc} of Fhy and Hem (i.e., small surface charges for both Hem and Fhy), the dispersion of Fhy aggregates by Hem became possible.

The effect of Hem nanoplates on the transformation of Fhy under different solution conditions

Transformation of Fhy in the presence of Hem nanoplates at different pH. The transformation rates and products of Fhy are highly pH-dependent. Hence, different pH conditions were chosen to investigate the effect of Hem surfaces on the transformation of Fhy.

First, our preliminary experiments showed that the mineral phase and the morphology of pure Hem nanoplates will not be changed after reacting at 75°C with different pH (Fig. S3), suggesting the high stability of Hem. Further experimental results demonstrated that the transformation process of Fhy was evidently affected by Hem nanoplates, and the effect varied with solution pH. According to the XRD patterns, pure Fhy transferred into Hem and Gth at pH 4, 7, and 12, but their reflection intensities were different, indicating various relative content of Hem and Gth in these samples (Fig. 1a-c). In specific, Fhy was primarily converted to Gth at pH 4 and 12, while at pH 7 the main products were Hem. Using the *k*-value method, the calculated relative content of Hem formed from pure Fhy at pH 4, 7, and 12 was 21.9 wt%, 69.7 wt%, and 14.5 wt%, respectively (Text S1 and Table S2). These results supported previous findings that neutral pH benefits the formation of Hem, whereas acidic and alkaline pH will favor the formation of Gth (Das et al. 2011b; Zhang et al. 2018).

In the presence of Hem nanoplates, the relative intensity of Hem reflections increased for the transformed products at different pH (Fig. 1d-f). The actual Hem contents in Fhy-20Hem-4-10d, Fhy-20Hem-7-10d, and Fhy-20Hem-12-24h were calculated to be 80.9 wt%, 79.0 wt%, and 49.2 wt%, respectively (Fig. S4a). We also calculated the theoretical Hem/(Hem+Gth) ratios at different pH, in which we assume that the added Hem will not affect the transformation process (i.e., these systems are denoted as Fhy+Hem, and the Hem contents were the sum of added Hem and produced Hem in pure Fhy transformation process, regarding as theoretical Hem contents). The calculation method was described specifically in Text S2, and the obtained values for the Fhy-20Hem systems at pH 4, 7, and 12 were 40.3 wt%, 75.9 wt%, and 34.5 wt%, respectively. Notably, the actual Hem contents in these samples (i.e., with the effect of Hem nanoplate) were higher than the corresponding theoretical contents, and the difference between these two contents (denoting as induced Hem) at different pH followed the order: pH 4 (40.6 wt%) > pH 12 (14.7 wt%) > pH 7 (3.1 wt%)

(Fig. S4a). These results confirmed the significant effect of Hem nanoplates in inducing the transformation of Fhy to Hem and the important role of solution pH in affecting the degree of Fhy transformation induced by Hem nanoplates.

MS was also utilized to characterize the final products and quantify the phase composition in these samples (Fig. 2). The obtained spectra were fitted to one doublet and two sextets, yielding relevant parameters consistent with those of Fhy (IS=0.23 mm/s, QS=0.82 mm/s), Hem (IS=0.36 mm/s, QS=-0.20 mm/s, B_{HF}=51 T), and Gth (IS=0.36 mm/s, QS=-0.26 mm/s, B_{HF}=37 T) (Murad, 1996; Cornell and Schwertmann 2003; Yan et al. 2020). The contents of Fhy, Hem, and Gth were calculated using the relative areas in the fitted spectra. The results showed that the residual Fhy contents at pH 4 and 12 were less than 5% (Fig. 2a, c, d, and f), suggesting the nearly complete transformation of Fhy in these samples. However, approximately 13.6% and 11.9% of Fhy remained untransformed in the Fhy-7-10d and Fhy-20Hem-7-10d samples, respectively (Fig. 2b and e), indicating the slower transformation kinetics at pH 7.

The fitting results revealed that pure Fhy (i.e., absence of Hem nanoplates) mainly converted to Gth at pH 4 (67.9%) and pH 12 (71.7%), while Hem was the main product (57.5%) at pH 7. The fitting ratios of Hem/(Hem+Gth) in the Fhy-20Hem-4-10d, Fhy-20Hem-7-10d, and Fhy-20Hem-12-24h samples were 76.2%, 70.5%, and 60.1%, respectively. Similar to above XRD results, here we used the MS results to calculate the theoretical Hem contents in various products by assuming that Hem nanoplate would not affect the transformation of Fhy, and the obtained values were 44.2%, 73.2%, and 41.2% in the Fhy-20Hem-4-10d, Fhy-20Hem-7-10d, Fh-20Hem-12-24h samples, respectively. These findings indicated that the actual Hem contents in Fhy-20Hem-4-10d (76.2%) and Fhy-20Hem-12-24h (60.1%) were much higher than their corresponding calculated theoretical contents (Fig. S4b), implying that the added Hem nanoplates induced the transformation of Fhy to Hem under

316 acidic and alkaline conditions. The induced Hem content was higher at pH 4 (32.0%) than
317 that at pH 12 (18.9%). At pH 7, the actual Hem content (70.5%) was just slightly lower than
318 the theoretical content (73.2%), suggesting that the added Hem nanoplates should have rather
319 weak effects on the transformation process. The MS results were consistent with above XRD
320 results, both confirmed the significant effects of added Hem in inducing the transformation of
321 Fhy under acidic and alkaline conditions, but weak at neutral pH.

322 The transformation kinetics of Fhy were further investigated by the ammonium oxalate
323 dissolution method, which revealed the complete transformation of pure Fhy at pH 4 (7 d)
324 and pH 12 (4 h) in the systems with or without Hem nanoplates (Fig. 3a and c); but at pH 7,
325 only 80 wt% of Fhy transformed even after 10 d's reaction (Fig. 3b). Besides, the obtained
326 results showed the accelerated transformation of Fhy by Hem nanoplates under acidic and
327 alkaline conditions (Fig. 3a and c), but not under neutral condition (Fig. 3b). For example,
328 only 10 wt% of Fhy remained untransformed in the presence of 20 wt% Hem nanoplates after
329 reacting for 3 d at pH 4, while 60 wt% of Fhy remained in the absence of Hem nanoplates
330 (Fig. 3a); at neutral pH, similar transformation rate of Fhy was obtained for the samples with
331 or without Hem nanoplates (Fig. 3b).

332 It is well-known that the transformation of Fhy under acidic and alkaline conditions
333 mainly proceeds through dissolution-recrystallization, whereas this process under neutral
334 conditions is mainly through solid-state transformation. Therefore, the induced
335 transformation of Fhy at pH 4 and 12 and the insignificant induced transformation of Fhy at
336 pH 7 indicated that Hem nanoplates might have influenced the dissolution-recrystallization of
337 Fhy during its transformation. Above results from the ammonium oxalate dissolution method
338 demonstrated that Hem nanoplates should have accelerated the transformation of Fhy through
339 affecting the balance of dissolution-recrystallization, which will be discussed in detail later.

340 **Transformation of Fhy with different Hem nanoplate contents.** The effect of Hem

nanoplate contents (i.e., Hem/(Fhy+Hem) = 0 wt%, 5 wt%, 10 wt%, 20 wt%, 40 wt%, or 70 wt%) on Fhy transformation at pH 4 was further investigated. The XRD analysis results revealed that the reflection intensities of Hem increased with rising Hem nanoplate contents. In specific, when the added Hem content reached 70%, only Hem reflections were observed after reacting for 10 days at pH 4, indicating that the predominant products were Hem, and the Gth content was below the detection limit of XRD (Fig. 4a). Hem and Gth contents were calculated based on the XRD reflection intensities using the *k*-value method. The obtained Hem contents were 35.4 wt%, 49.0 wt%, 67.6 wt%, 91.7 wt%, and 100 wt% for the samples with 5 wt%, 10 wt%, 20 wt%, 40 wt%, and 70 wt% Hem nanoplates, respectively, which were higher than the corresponding theoretical contents of 29.4 wt%, 33.3 wt%, 41.1 wt%, 56.4 wt%, and 78.6 wt% (Fig. 4b). Clearly, the degree of Hem-induced transformation of Fhy increased with rising Hem nanoplate contents (Table S2), and the mechanisms will be discussed in detail later.

Above kinetics data showed that the Hem nanoplates could accelerate Fhy transformation at pH 4, particularly after reacting for 3 d (Fig. 3a). Hence, the residual Fhy content in the samples with different Hem nanoplate contents after reacting at pH 4 for 3 d was calculated using the ammonium oxalate dissolution method. The obtained results also showed that the residual Fhy contents decreased with rising Hem nanoplate contents, and Fhy was nearly completely transformed when the original Hem nanoplate concentration exceeded 40 wt% (Fig. 4b). This phenomenon further proved that the transformation rate of Fhy will increase with rising Hem nanoplate contents.

The structural characteristics of the transformed products under acid and neutral conditions

The obtained samples after reacting for 10 days at pH 4 and 7 were first characterized by SEM. In the pure Fhy systems, Fhy was found to mainly transform into short rod-like Gth at

pH 4 (Fig. 5a), whereas at pH 7, it mainly transformed into granulous Hem and a small number of acicular Gth (Fig. 5c). When 20 wt% Hem nanoplates were present during the transformation process, the newly formed Gth and Hem exhibited similar morphology as those in the pure Fhy systems, whereas the added Hem nanoplates changed their original morphology, especially at pH 4 (Fig. 5b). In specific, the flat {001} facets of Hem nanoplates became coarse and grew in the form of islands at pH 4 (Fig. 5b). Similar growth characteristics were observed by Yanina and Rosso (2008) and Rosso et al. (2010), and the authors found that the large Hem pyramids nucleated as islands at the initially flat {001} surface of Hem in the presence of 1 mM Fe^{2+} and 10 mM oxalic acid.

The morphology of the final products with different Hem nanoplate contents was further characterized by SEM (Fig. S5). In the system with 5 wt% Hem nanoplates at pH 4, the products after aging for 10 d (i.e., Fhy-5Hem-4-10d) exhibited similar morphology as that of Fhy-20Hem-4-10d (Fig. 5b and Fig. S5a). With the content of Hem nanoplates increasing to 70 wt%, the products were predominately composed of Hem without the observation of rod-like Gth (Fig. S5b), consistent with the above XRD results. In Fhy-5Hem-4-10d and Fhy-20Hem-4-10d, only island growth at the {001} facets of Hem nanoplates was observed (Fig. S5a and Fig. 5b); whereas in Fhy-70Hem-4-10d, layer-by-layer growth was also observed at the {001} facets of Hem nanoplates besides the island growth (Fig. S5b). The morphology of Hem nanoplates reacted at pH 7 remained largely unchanged (Fig. 5d), with slight growth being observed at the flat {001} facet (the inset in Fig. 5d), which indicated that the Hem nanoplates just have slightly induced the transformation of Fhy to Hem, and the growth mode was similar to that in Fhy-20Hem-4-10d (i.e., island growth).

As just a slight induced transformation of Fhy to Hem was observed at pH 7 and the growth characteristics of Hem at its {001} facets at pH 7 were similar to those at pH 4, only the products formed at pH 4 for different times were analyzed to reveal the growth process of

Hem nanoplates (Fig. 6). The SEM images of Fhy-20Hem-4, taken at different reaction intervals, clearly showed the gradual growth of {001} facets of Hem nanoplates during Fhy transformation (Fig. 6a and b). SEM images revealed that the {001} facets of the original Hem nanoplates were smooth (Fig. $6b_1$), whereas those of the reacted Hem nanoplates became rough (Fig. $6b_2$-b_6). From the side view, the reacted Hem nanoplates displayed jagged edges (Fig. S6a), which were distinct from the original flat edges (Fig. S6b). Moreover, the size distribution histograms of the Hem nanoplates were calculated using more than 100 particles in the TEM images (the inset in Fig. 6d and e), which showed that the average width of the original Hem nanoplates and reacted Hem nanoplates was 179.2 ± 20.8 and 215.1 ± 20.3 nm, respectively. This phenomenon demonstrated that the side facets of Hem nanoplates also grew during Fhy transformation, but their growth mode may differ from that of {001} facets. In specific, the side facets of Hem nanoplates remained smooth during the transformation of Fhy (Fig. 6b), suggesting a layer-by-layer growth mode.

With the further growth of Hem nanoplates, the {001} facets disappeared completely and the initial hexagonal nanoplates transformed into pseudo-cubes (Fig. 6a and b). These pseudo-cubic nanocrystals exhibited structural features following the geometric model of an ideal rhombohedron enclosed by {012} facets (Fig. $6a_6$). The SEM images showed that the sharp edges of the horizontally lying Hem nanoplates became rounded during the transformation, matching with the combination of {113}, {012}, and {001} facets (Fig. $6a_1$, a_3, and b). The intersections of side facets (Fig. $6a_2$, and c) and the morphology of reacted Hem nanoplates from the side view (Fig. $6a_4$ and b_3) were also consistent with the combination of {113}, {012}, and {001}. These results demonstrated that the {113} facets of Hem nanoplates gradually grew to form {012} facets during the transformation, and ultimately, the twelve {113} facets were replaced by six {012} facets. The morphology and structure of Fhy-20Hem-4-10d were further analyzed by TEM and HRTEM (Fig. 6f-h). The

HRTEM results confirmed that the short rod-like iron oxide was Gth (Fig. 6g), and the {001} facets of reacted Hem nanoplates became rough (Fig. 6f), showing an island growth mode. Moreover, the FFT analysis demonstrated that the Hem pyramids growing at the initially flat {001} facets were still along the [001] zone axis (Fig. 6h).

The structural characteristics of the transformed products under alkaline conditions

The products that underwent a reaction at pH 12 were initially characterized by SEM. For the pure Fhy samples, acicular and tabular Gth were primarily formed, along with a small amount of granulous Hem (Fig. 5e). These products were also observed in the sample with the presence of Hem heterogeneous surfaces (Fig. 5f). Notably, the morphology of Hem nanoplates underwent significant changes after reacting for 24 h at pH 12, which differed greatly from the morphologies of the reacted Hem nanoplates under acidic and neutral conditions. Flower-like iron oxides were formed, with the hexagonal nanoplates presenting at the center (Fig. 5f), which indicated that the new iron oxides might utilize Hem nanoplates as templates during their growth. SEM images further revealed that the {001} facets of Hem nanoplates grew mainly layer-by-layer (Fig. S7a), which was markedly different from the growth mode of {001} facets observed in the presence of 20 wt% Hem nanoplates under neutral and acidic conditions.

The mineral phases of the flower-like sample were further characterized using TEM and HRTEM (Fig. 7). TEM images well displayed the flower-like morphology of the product (Fig. 7a). The HRTEM images and corresponding FFT patterns revealed that the petals of the flower were composed of Gth orienting along the [$\bar{2}$00] zone axis (Fig. 7b-d and f). The center of the flower consisted of Hem nanoplates that oriented along the zone axis of [001] (Fig. 7d and e). The FFT patterns demonstrated that the facets of Hem and Gth had a close correlation, i.e., Hem ($\bar{1}\bar{1}$0)// Gth (021), Hem (1$\bar{2}$0) // Gth (040), and Hem (2$\bar{1}$0) // Gth (02$\bar{1}$).

Furthermore, the HRTEM image exhibited continuous lattice fringes between the central Hem and the petal Gth (Fig. S7b and c), which can be attributed to a lattice match between Hem and Gth crystals. Based on these facets mentioned above, the structures of Hem and Gth were simulated through Material Studio and Crystalmaker (Fig. 7g and h). The spatial positions of oxygen and iron atoms in the bulk structure of Hem and Gth were found to be very close from the perspective of Hem [001] and Gth [$\bar{2}$00]. Since the exposed edge facets of the original Hem nanoplates were {113}, we sliced the (113) facet on the Hem supercell, and found that the ($\bar{1}2\bar{1}$)) facet of Gth supercell was parallel to Hem (113) facet. To evaluate the structure of the facets of the two crystals more intuitively, the atoms in the facets of the two crystals were put together (Fig. 7g and h). Clearly, the spatial positions of the oxygen and iron atoms were quite similar for Hem and Gth from different perspectives (i.e., a very small lattice mismatch) (Fig. 7g and h). These results demonstrated that Hem nanoplates can act as templates for the heteroepitaxial growth of Gth during the transformation of Fhy under alkaline conditions.

DISCUSSION

Dissolution-recrystallization controlled transformation of Fhy at Hem surfaces

Numerous studies have concerned the phase transformation of metastable phases in the absence of heterogeneous surfaces, and direct solid-state transformation and dissolution-recrystallization transformation are the main pathways (Das et al. 2011a, b; Jiang et al. 2018b). Theoretically, the presence of heterogeneous surfaces may affect both of these two pathways through surface interactions. (1) Heterogeneous surfaces may directly interact with metastable particles to induce solid-state transformation (Riechers et al. 2017; Wu et al. 2023). This process shows similarity to non-classical crystallization, as both use the preformed metastable intermediate particles as crystallization precursors and involve solid-state

transformation. Riechers et al. (2017) proposed that calcite surface can induce the direct solid-state transformation of amorphous cadmium carbonate into otavite, which was ascribed to the lower interfacial energy between otavite and calcite substrate (because of their similar crystal structure) than that between precursor phase and calcite substrate. (2) During the dissolution-recrystallization process, the dissolved ions from metastable particles, like any other ions in solution, can nucleate at the heterogeneous surfaces due to the lower nucleation energy barrier, which may accelerate the crystallization process and even alter the crystallization pathway. For example, during the Fe^{2+}-catalyzed transformation of Fhy/lepidocrocite (Lep), Fe^{2+} could exchange electrons with Fhy/Lep to accelerate the dissolution of Fe^{3+}, which would benefit the dissolution-recrystallization transformation pathway (Notini et al. 2022; Liu et al. 2022a). The presence of Gth surfaces affected the Fe^{2+}-catalyzed transformation process of Fhy/Lep through the surface-induced nucleation and recrystallization of dissolved Fe^{3+}, and Gth became the major transformed product while other products (e.g., Lep, Mag) were inhibited.

In this work, the transformation experiments were conducted at relatively high temperature and under different pH environments, and both the dissolution-recrystallization and solid-state transformation of Fhy occurred in the pure Fhy systems (Fig. 5a, c, and e). In the systems with added Hem nanoplates, we observed not only new individual Hem/Gth particles, but also the induced growth of Hem/Gth at the surfaces of Hem nanoplates, particularly under acidic and alkaline conditions (Fig.5b, d, and f). These results suggested that the transformation pathway of Fhy had been partly altered by the added Hem nanoplates. Clearly, the different transformation pathways, including the direct transformation to Hem/Gth and the surface-induced transformation to Hem/Gth, will compete with each other, while the ratio of these final products depends on the reaction conditions (e.g., solution pH, Hem contents, and exposed facets). As the direct transformation of pure Fhy has been well

documented in previous studies (Cornell and Schwertmann 2003; Das et al. 2011b; Jiang et al. 2018b), here we will focus on the induced transformation pathways at Hem surfaces.

Although heterogeneous surfaces may affect the transformation of metastable phases through both the direct solid-state transformation and the dissolution-recrystallization pathways (Riechers et al. 2017; Notini et al. 2022; Liu et al. 2022a). We propose that the transformation of Fhy at Hem surface is more likely controlled by the later pathway due to the following reasons. (1) As shown in this work and previous studies (Shaw 2005; Das et al. 2011b), the dissolution-recrystallization transformation of pure Fhy into Gth is always an important pathway in hydrothermal reaction systems, particularly under acidic and alkaline conditions. Theoretically, the dissolved Fe^{3+} ions from Fhy can recrystallization at the surfaces of Hem nanoplates due to the lower nucleation energy barrier, similar to the Fe^{2+}-catalyzed transformation of Fhy/Lep in the presence of Gth (Notini et al. 2022; Liu et al. 2022a). (2) Our experimental results showed the facet-specific growth of Hem/Gth at the surfaces of Hem nanoplates, and the growth was more evident at pH 4 and pH 12 than at pH 7 (Fig. 5), in accordance with the dissolution capacity of Fhy (i.e., contents of dissolved Fe^{3+}) at different pH. Cornell and Schwertmann (2003) reported the activity of dissolved Fe ($\log\alpha_{Fe}$) to reflect the solubility of Fhy and higher solubility of Fhy at pH 4 (-5.96) and pH 12 (-6.07) than that at pH 7 (-9.11). Besides, with rising Hem nanoplate contents at pH 4 (i.e., increasing heterogeneous surfaces for the recrystallization of dissolved Fe^{3+}), both the transformation rate of Fhy and the growth of induced Hem increased (Fig. 4). Above results in combination suggested the dissolution of Fe^{3+} from Fhy and the induced growth of new crystals at the surfaces of Hem nanoplates. (3) The solid-state transformation of Fhy mainly involves the structural rearrangement of atoms within Fhy particles (Solits et al. 2016; Yan et al. 2021; Wei et al. 2023). The relatively weak surface interactions between Fhy and Hem particles, due to their similar surface charges, resulted in the formation of Fhy aggregates instead of

515 well dispersed Fhy/Hem composites (Fig. S2), and thus the weak surface interactions
516 between Hem and Fhy particles should hardly induce the rearrangement of atoms within Fhy
517 particles to cause direct solid-state transformation. Theoretically, the strong interactions
518 between heterogeneous surfaces and metastable particles, in combination with the low energy
519 barrier for solid-state transformation, will benefit the surface-induced solid-state
520 transformation, such as the transformation of amorphous cadmium carbonate into otavite at
521 calcite surfaces (Riechers et al. 2017). In all, we propose that in this work Fhy likely
522 functions as the Fe^{3+} source in solution, and Hem surfaces can well induce the
523 recrystallization of dissolved Fe^{3+}.

524 The Hem nanoplate surfaces, by affecting both the dissolution of Fhy and the
525 recrystallization of dissolved Fe^{3+}, can not only promote the transformation process, but also
526 change the transformed products (Fig. 3 and Fig. 8). On one hand, like other heterogeneous
527 crystallization processes, the preexisting Hem nanoplates can provide heterogeneous surfaces
528 for the crystallization of dissolved Fe^{3+} (Fig. 8c), which subsequently will accelerate the
529 consumption of dissolved Fe^{3+} and promote the dissolution of Fhy through influencing its
530 dissolution equilibrium. As such, the presence of Hem nanoplates accelerated the
531 transformation rate of Fhy, particularly under acidic and alkaline conditions where Fhy has a
532 larger dissolution capacity (Fig. 3a and c). With rising Hem nanoplate contents, the
533 consumption of dissolved Fe^{3+} by Hem nanoplates became more significant, which then
534 resulted in significantly accelerated transformation rates of Fhy (Fig. 4b). On the other hand,
535 the surfaces of Hem nanoplates can serve as templates for the nucleation of dissolved Fe^{3+}
536 during the growth of crystals, and the template effect (or lattice matching) plays an important
537 role in modulating the type and morphology of the transformed products (Fig. 6 and 7).
538 Generally, the template effect will lead to the preferential growth of crystals with the same or
539 similar crystal structure as the substrate to achieve a small lattice mismatch (Riechers et al.

2017, 2022). As such, it is reasonable to observe the induced growth of Hem in all of the studied systems. The heteroepitaxial growth of Gth at pH 12 might be attributed to the high concentration of OH^- and the high supply of Fe^{3+}, which favors the growth of Gth (Shaw, 2005; Cudennec and Lecerf 2006; Das et al. 2011b; Chen 2021). The Hem nanoplates can still serve as templates for the growth of Gth at specific directions due to the small lattice mismatch between the specific directions of these two minerals, i.e., [001] direction of Hem and [$\bar{2}$00] direction of Gth (Fig. 7g and h), thus promoting the heteroepitaxial growth of Gth at Hem surfaces. Besides, the induced growth of crystals also strongly depends on various reaction factors, such as solution pH, the exposed facets, and the added contents of Hem. The underlying mechanisms of how various factors modulate the transformation of Fhy will be further discussed hereinafter.

Factors affecting the recrystallization of dissolved Fe^{3+} at the surfaces of Hem nanoplates

Our results demonstrated that the surfaces of Hem nanoplates can affect the transformation behaviors of Fhy mainly through the dissolution-recrystallization pathway. As the dissolution of Fe^{3+} from Fhy is primarily determined by solution pH (Cornell and Schwertmann 2033; Das et al. 2011b), we will, therefore, mainly focus on the complex recrystallization process of dissolved Fe^{3+}. Theoretically, the presence of heterogeneous surfaces can reduce the nucleation energy barrier and promote the heterogeneous crystallization of ions (Hu et al. 2013; Khaleghi et al. 2020; Wu et al. 2020), which are strongly affected by both solution conditions (e.g., solution pH, ion concentration) and the physicochemical properties of heterogeneous surfaces (e.g., atomic structure, surface charge) (Dai and Hu 2015; Xu et al. 2014b; Callagon et al. 2017; Sheng et al. 2021; Yang et al. 2023). Sheng et al. (2021) found that during the Fe^{2+}-catalyzed transformation of Fhy, the concentration of solution labile Fe^{3+} (an intermediate species), plays an important role in

565 controlling the crystallization pathways. Low supersaturation of labile Fe^{3+} can favor the
566 heterogeneous crystallization of Gth, whereas increasing labile Fe^{3+} supersaturation will
567 promote the homogeneous crystallization of Gth. Hu et al. (2013) observed the faster
568 heterogeneous nucleation of iron (oxyhydr)oxides on corundum compared with that on quartz
569 and muscovite, which can be ascribed to the smaller lattice mismatch between corundum and
570 iron (oxyhydr)oxide, resulting in lower interfacial energy. In this study, the complicated
571 heterogeneous crystallization processes controlled by various factors (e.g., solution pH, the
572 crystallinity of Fhy, the added Hem contents, and the exposed Hem facets) were also
573 observed.

574 Solution pH can influence both the dissolution of Fhy and the homogeneous
575 crystallization of dissolved Fe^{3+} (Schwertmann and Murad 1983; Das et al. 2011b). The
576 acidic and alkaline conditions will promote the dissolution of Fhy to produce high contents of
577 Fe^{3+}, and high solution pH will favor the homogeneous crystallization of solution Fe^{3+} into
578 Gth (Cornell and Schwertmann 2003; Zhang et al. 2018; Chen 2021). In a heterogeneous
579 crystallization process, the crystallization behaviors strongly depend on the local
580 concentration of ions at substrate surfaces (Jung and Jun 2016; Riechers et al. 2022), which,
581 in this work, can be easily modulated by solution pH. At pH 7, the extremely weak solubility
582 of Fhy leads to low Fe^{3+} concentration at Hem surfaces and slow crystallization as well, and
583 thus the template effects (or lattice matching) will induce the preferential growth of Hem over
584 Gth. Besides, the low Fe^{3+} concentration also suggests the low content of induced Hem, and
585 thus the direct solid-state transformation into Hem is the dominant pathway in this system
586 (Fig. 1b and e, Fig. S4). At pH 4, the large solubility of Fhy results in high Fe^{3+} concentration
587 both in solution and at Hem surfaces, and the template effects of Hem surfaces then help the
588 recrystallization of Fe^{3+} into induced Hem, with the content much higher than that at pH 7.
589 The dominant transformation product, therefore, changes from Gth to Hem with the addition

590 of Hem nanoplates (Fig. 8a). On the other hand, the high solubility of Fhy and high OH^-
591 concentration at pH 12 leads to rather quick dissolution and transformation of Fhy (Fig. 1c).
592 Although the template effects can still contribute to the heterogeneous crystallization of Hem,
593 the simultaneous presence of high concentrations of both Fe^{3+} and OH^- causes the favorable
594 growth of Gth in the solution or at Hem surfaces due to the lower free energy barrier for the
595 formation of Gth than that of Hem under alkaline conditions (Das et al. 2011b; Chen 2021);
596 these two factors jointly cause the lower ratio of induced Hem at the surfaces of Hem
597 nanoplates at pH 12 than that at pH 4 (Fig. 8a). Similar concentration-controlled
598 heterogeneous crystallization behaviors were also reported by Riechers et al. (2022). They
599 found that a low Co^{2+} concentration could benefit the heterogeneous crystallization of $CoCO_3$
600 on magnesite; whereas a high initial Co^{2+} concentration will promote the heterogeneous
601 crystallization of $Co(OH)_2$ on magnesite.

602 Changing the Hem nanoplate contents can alter the availability of heterogeneous
603 surfaces, which could further affect the heterogeneous crystallization of dissolved Fe^{3+}. Our
604 results show that the rising content of Hem nanoplates at pH 4 results in the accelerated
605 transformation rate of Fhy and the increased growth of induced Hem (through template
606 effects), which is well in accordance with the increased heterogeneous surfaces for the
607 recrystallization of Fe^{3+}. Moreover, the induced Hem even becomes the dominant
608 transformation product for Fhy at high Hem nanoplate contents (Fig. 4). These results support
609 that Hem surfaces can well induce the transformation of Fhy through template effects. In
610 addition, our results show that the low concentration of Fe^{3+} at Hem surfaces, which can be
611 achieved by modulating solution pH (e.g., low solubility of Fhy at neutral pH) and added
612 Hem nanoplate content (e.g., more available heterogeneous surfaces), will always favor the
613 formation of induced Hem, suggesting better template effects at lower Fe^{3+} concentration.

614 Drying treatment can enhance the crystallinity of Fhy and thus reduce its solubility

(Lewis 1992), providing an additional method to modulate Fe^{3+} concentration. The transformation of dried Fhy in the systems with or without Hem nanoplates was conducted at pH 12 (Text S3 and Fig. S8). Our results confirmed the much slower transformation of Fhy after drying treatment (Fig. 1c and Fig. S8a). Notably, we observed the absence of induced growth of Gth at the surfaces of Hem nanoplates (Fig. S8d), very different from the systems with undried Fhy (Fig. 5f), which provides additional evidences verifying above hypothesis that the low surface concentration of Fe^{3+} will benefit the induced growth of Hem through better template effects.

Interestingly, our results show that the recrystallization of dissolved Fe^{3+} at Hem surfaces is highly facet-specific (Fig. 6 and 7). Several studies have also revealed that the heterogeneous crystallization of ions can be facet-specific (Wu et al. 2021; Liu et al. 2021a; Huang et al. 2023). For example, Liu et al. (2021a) found the preferential catalytic oxidation of Mn(II) and growth of manganese oxides at the {113} facets over {001} facets of Hem nanoplates, and the authors proposed that the different atomic structures at various facets of Hem nanoplates led to the difference of adsorption and catalytic redox of solution ions, induced-nucleation energy, and lattice mismatch, resulting in facet-specific crystallization behaviors. Our study, for the first time, observes not only the different growth modes of Hem (i.e., island growth, layer-by-layer growth; will be discussed in detail later), but also the different induced products (i.e., Hem, Gth) at various facets (Fig. 6 and 7). Similarly, we propose that the different atomic arrangement of {001} and {113} facets should be the reason for the obtained facet-specific induced products. In specific, the {001} facets with inert doubly-coordinated hydroxyls (Barrón and Torrent 1996; Chatman et al. 2013) will lead to weak adsorption of Fe^{3+} and thus low surface Fe^{3+} concentration, which could benefit the induced growth of Hem at Hem {001} facets due to the better template effects as discussed above. On the other hand, the {113} facets with highly reactive singly-coordinated oxygens,

640 which generally show a better adsorption capacity toward metal ions (Voelz et al. 2018; Liu
641 et al. 2021a), can obtain higher concentration of Fe^{3+} at Hem {113} facets, resulting in the
642 heteroepitaxial growth of Gth due to its lower formation free energy than that of Hem at pH
643 12 (i.e., the formation of Hem through template effects being inhibited). In addition,
644 increasing Hem nanoplate contents (i.e., 70%) at pH 12 was applied to decrease the surface
645 concentration of Fe^{3+}. Rather weak Gth reflections and the absence of heteroepitaxial growth
646 of Gth at Hem surfaces were also observed (Fig. S9). These results further confirmed that the
647 surface concentration of Fe^{3+} is rather important in controlling the induced products at Hem
648 surfaces.

649 **The competition between various transformation pathways**

650 As shown above, solid-state transformation, homogeneous crystallization, and
651 heterogeneous crystallization were observed during the transformation of Fhy in the presence
652 of Hem nanoplates (Fig. 8c). Although the Hem surfaces mainly affect the transformation of
653 Fhy through dissolution-recrystallization and then induce the growth of Hem/Gth from the
654 dissolved Fe^{3+}, the solid-state transformation of Fhy could be also affected during the
655 transformation process. In specific, the quick consumption of dissolved Fe^{3+} by the induced
656 growth of Hem/Gth would in turn promote the dissolution of Fhy, which subsequently will
657 weaken the direct solid-state transformation of Fhy. For example, we observed the absence of
658 Hem particles formed from the solid-state transformation in Fhy-70Hem-4-10d (Fig. S5),
659 because the induced formation of Hem was enhanced with increasing Hem nanoplate
660 contents.

661 Besides, the competition between homogeneous crystallization and heterogeneous
662 crystallization, both using dissolved Fe^{3+} as the monomer, is also observed (Fig. 8c).
663 According to the classical nucleation theory, supersaturation of precursors controls both
664 homogeneous crystallization and heterogeneous crystallization. At low supersaturation of

665 monomers, heterogeneous crystallization will be more favorable due to its lower nucleation
666 energy barrier than homogeneous crystallization; with increasing the supersaturation of
667 monomers, homogeneous crystallization will be enhanced (Jung and Jun 2016; Sheng et al.
668 2021). Nguyen et al. (2011) applied magnetite seed to synthesize magnetite and
669 gold/magnetite nanoparticles. The authors found that a high concentration of monomers (i.e.,
670 Fe^{2+}, Au^{3+}) will promote the generation of small particles through homogeneous
671 crystallization, which will compete for monomers with the added magnetite seeds (i.e.,
672 heterogeneous crystallization). Similarly, in our study, in addition to the heterogeneous
673 crystallization of Gth at Hem surfaces to consume the dissolved Fe^{3+}, the higher
674 supersaturation of Fe^{3+} at pH 12 (as compared with that at pH 4) promotes the homogeneous
675 crystallization of Fe^{3+} to Gth, resulting in the weaker induced transformation of Fhy to Hem
676 (Fig. 8a).

677 **The continuous growth of Hem nanoplates during the transformation of Fhy**

678 The induced transformation of Fhy to Hem can be evidenced by the continuous growth
679 of added Hem nanoplates, and different growth modes (i.e., island growth, layer-by-layer
680 growth) were observed (Fig. 5, Fig. 8b, and c). We propose these growth modes are
681 controlled by the concentration of Fe^{3+} at Hem surfaces, which is closely related to the
682 solubility of Fhy and the affinity of Hem facets toward Fe^{3+}. The relatively low solubility of
683 Fhy (e.g., at pH 4 and pH 7) led to a low concentration of Fe^{3+} in solution. The surface
684 concentration of Fe^{3+} at {001} facets, due to its relatively weak adsorption capacity (Voelz et
685 al. 2018; Liu et al. 2021a), should be low, which then resulted in island growth mode (Fig. 8b
686 and c); while the high affinity of Hem {113} facets toward Fe^{3+} could result in high surface
687 concentration of Fe^{3+} and then benefit the layer-by-layer growth (Fig. 6b). The accelerated
688 dissolution of Fhy at pH 12 enhances the supply of Fe^{3+}, leading to a high concentration of
689 Fe^{3+} at Hem {001} facets, and then further resulted in layer-by-layer growth mode (Fig. S7a).

690 Demianets et al. (2003) also reported a similar Fe^{3+} concentration-controlled growth mode of
691 Hem, in which Fe^{3+} was dissolved from the chemical-grade Fe_2O_3 and its concentration was
692 controlled by different hydrothermal temperatures and ionic type. They found that the layer-
693 by-layer growth of Hem is the main growth mode for Hem at high Fe^{3+} supply content, while
694 island growth mode becomes obvious at low Fe^{3+} concentration.

695 Another intriguing observation is the morphological evolution of Hem nanoplates
696 caused by their continuous growth during the transformation of Fhy. At pH 4, the morphology
697 of added Hem nanoplates gradually evolved from hexagonal nanoplates to pseudo-cubic
698 shape during Fhy transformation, which suggests the replacement of twelve {113} facets by
699 six {012} facets and the disappearance of {001} facets (Fig. 6a and b). The growth of crystals
700 is a complicated process and is mainly controlled by the atomic configuration and the surface
701 energy of the exposed facets. The BFDH (Bravais-Friedel-Donnay-Harker) law predicts that
702 crystal morphology should be dominated by slow-growing facets (i.e., those facets with
703 higher reticular density or larger inter-planar distances), and the facets with smaller planar
704 distance will grow faster and thus disappear first (Prywer 2004; Guo and Barnard 2011). For
705 the growth of side facets of Hem nanoplates, the interplanar distance of Hem {012} facets
706 (0.37 nm) is larger than that of {113} facets (0.22 nm), suggesting that the {012} facets
707 should grow slower and can be reserved during their growth. On the other hand, previous
708 studies have revealed that the average surface energy of Hem {012} facets is lower than that
709 of {113} facets (Ouyang et al. 2014), demonstrating that {012} facets are thermodynamically
710 more stable than {113} facets, and the transition from {113} facets to {012} facets during the
711 growth of Hem nanoplates is theoretically more favorable. As for the growth of Hem {001}
712 and {012} facets, it is worth noting that the surface energy of {001} facets (4.88 $J \cdot m^{-2}$) is
713 greater than that of {012} facets (3.12 $J \cdot m^{-2}$) (Stirner et al. 2020), indicating that {012} facets
714 are more stable and therefore more likely to be retained during the growth process. Guo and

Barnard (2011) have also revealed that the pseudo-cubic shape of Hem is the thermodynamically preferred shape at all sizes due to its lower free energy. Consequently, Hem nanoplates tend to form pseudo-cubes during their slow growth process.

The morphology of Hem nanoplates remains largely unchanged at pH 12, and they still consist of hexagonal nanoplates as single crystals or at the center of flower-like iron oxides (Fig. 5f and Fig. S7a). According to the Thomson-Gibbs equation, higher supersaturation is conducive to the formation of facets with higher surface energy (i.e., {113} and {001} facets) (Lin et al. 2013; Ouyang et al. 2014). In other words, the high supersaturation at pH 12 (high concentration of Fe^{3+} and OH^-) in this work could benefit the retention of {001} and {113} facets of Hem nanoplates. These findings suggest that the morphology evolution of Hem nanoplates is controlled by both the thermodynamic and kinetic factors, i.e., surface energy and monomer concentration.

IMPLICATIONS

In this work, we studied the transformation behaviors of metastable Fhy in the presence of heterogeneous surfaces provided by Hem nanoplates. Our findings have at least the following geochemical significances. First, this work provides novel information for understanding the phase transformation behaviors of Fhy in the nature. The transformation of Fhy is a critical step for the formation of stable iron oxides at near-surface environments and plays a crucial role in controlling the biogeochemical cycles of coexisting ions (Hochella et al., 2005; Sakakibara et al. 2019; Kappler et al. 2021; Caraballo et al. 2022; Liu et al. 2021b, 2022b). Previous studies have shown that the transformation process of Fhy can be accelerated in the presence of reducing matters (e.g., Fe^{2+}) by enhancing the reduction-induced dissolution of Fhy (Hansel et al. 2005; Loan et al., 2005; Yee et al. 2006; Liu et al. 2022a), while non-reducing materials (e.g., ions, organic molecules, clay minerals, etc.) always decrease the transformation rate of Fhy through stabilizing the Fhy structure or

740 dispersing the Fhy aggregates (Das et al. 2011a; Cismasu et al. 2014; Yan et al. 2020, 2021;
741 Wei et al. 2023). Our study shows that the coexisting Hem nanoplates, by providing
742 heterogeneous surfaces for the induced crystallization of dissolved Fe^{3+} from Fhy, can
743 evidently accelerate the transformation of Fhy under acidic and alkaline conditions through
744 affecting its dissolution-recrystallization process, and the induced crystallization products at
745 Hem surfaces can be Hem or Gth, depending on solution pH and exposed Hem facets. We
746 can expect that other coexisting minerals (particularly iron oxides), as long as they can
747 provide heterogeneous surfaces for the induced crystallization of dissolved Fe^{3+}, will always
748 affect the transformation process of Fhy. Our findings, in combination with previous studies,
749 well demonstrate the complex transformation behaviors of Fhy in the nature.

750 Results from this study also shed new light on understanding the complex mechanisms
751 of heterogeneous surfaces in controlling the transformation of metastable precursors. Several
752 previous studies have found that heterogeneous surfaces can affect the transformation
753 behaviors of metastable precursors, through induced solid-state transformation or dissolution-
754 recrystallization processes (Politi et al. 2008; Dey et al. 2010; Riechers et al. 2017; Notini et
755 al. 2022; Liu et al. 2022a). This work comprehensively studied the effects of various factors
756 (e.g., solution pH, Hem content, exposed facets of Hem) on the surface-induced
757 transformation behaviors of metastable Fhy, and the transformation kinetics and final
758 products were well characterized. Our results, for the first time, demonstrate that the exposed
759 facets of Hem together with the supply of dissolved Fe^{3+} from Fhy control the heterogeneous
760 crystallization products at Hem surface, e.g., the recrystallization of Fe^{3+} to form Hem at
761 Hem {001} facets, while heteroepitaxial growth of Gth at {113} facets at pH 12. Above
762 findings collectively showed the complexity of heterogeneous surfaces in modulating the
763 crystallization process of minerals. Considering the ubiquity of heterogeneous surfaces and
764 metastable phases in the nature, more researches are needed to fill the knowledge gaps.

765 Finally, this study reveals that the preexisting Hem can alter the transformation pathway
766 of Fhy in the nature, which may help the inversion of geological environments. It is
767 recognized that Hem forms in high temperature and limited rainfall environments, while Gth
768 forms in low temperature and continuously wet conditions (Cudennec and Lecerf 2006; Das
769 et al. 2011b; Zhang et al. 2018). As such, the Hem/(Hem+Gth) ratio can vary in response to
770 changing climate conditions and has been regarded as a useful indicator for investigating soil
771 moisture regimes and pedogenesis (Hyland et al. 2015; Zhao et al. 2017; Silva et al. 2020).
772 Nevertheless, our results demonstrate that the presence of Hem nanoplates can enhance the
773 Hem formation under acidic and alkaline conditions, which is believed to favor Gth
774 formation during the transformation of Fhy in the absence of Hem nanoplates. As such, the
775 induced transformation of Fhy by Hem may alter the Hem/(Hem+Gth) ratios in soils and
776 sediments. Indeed, Hem is the most stable iron oxide and can be preserved for a long
777 geological time (Hoashi et al. 2009), during which the regional supergene environments may
778 experience significant change, e.g., evolving from favoring the formation of Hem to that of
779 Gth. In this term, the preexisting Hem may cause a larger Hem/(Hem+Gth) ratio, which
780 should be taken into consideration during the inversion of actual environmental changes.

781 **ACKNOWLEDGEMENTS AND FUNDING**

782 This study was supported by the National Science Fund for Distinguished Young
783 Scholars (Grant No. 42225203), National Natural Science Foundation of China (Grant No.
784 42272045 and 42302033), Youth Innovation Promotion Association CAS (Grant
785 No.2020347), Guangdong Major Project of Basic and Applied Basic Research (Grant No.
786 2023A04J0904), Science and Technology Planning Project of Guangdong Province (Grant
787 No. 2023B1212060048), Natural Science Foundation for Distinguished Young Scientists of
788 Guangdong Province (Grant No. 2023B1515020006), The Science and Technology
789 Development Fund of Macau (FDCT-22-037-SSI, 0070/2022/A).

REFERANCES CITED

Addadi, L., Raz, S., and Weiner, S. (2003) Taking Advantage of Disorder: Amorphous Calcium Carbonate and Its Roles in Biomineralization. Advanced Materials, 15, 959–970.

Barrón, V., and Torrent, J. (1996) Surface Hydroxyl Configuration of Various Crystal Faces of Hematite and Goethite. Journal of Colloid and Interface Science, 177, 407–410.

Callagon, E.B.R., Lee, S.S., Eng, P.J., Laanait, N., Sturchio, N.C., Nagy, K.L., and Fenter, P. (2017) Heteroepitaxial growth of cadmium carbonate at dolomite and calcite surfaces: Mechanisms and rates. Geochimica et Cosmochimica Acta, 205, 360–380.

Caraballo, M.A., Asta, M.P., Perez, J.P.H., and Hochella, M.F.Jr. (2022) Past, present and future global influence and technological applications of iron-bearing metastable nanominerals. Gondwana Research, 110, 283–304.

Chan, J.Y.T., Ang, S.Y., Ye, E.Y., Sullivan, M., Zhang, J., and Lin, M. (2015) Heterogeneous photo-Fenton reaction on hematite (α-Fe_2O_3) {104}, {113} and {001} surface facets. Physical Chemistry Chemical Physics, 17, 25333–25341.

Chatman, S., Zarzycki, P., and Rosso, K.M. (2013) Surface potentials of (001), (012), (113) hematite (α-Fe_2O_3) crystal faces in aqueous solution. Physical Chemistry Chemical Physics, 15, 13911.

Chen, S. 2021. The formation of iron (hydr)oxides in surface environments: a crystallographic and kinetic study. The Pennsylvania State University.

Cismasu, A.C., Michel, F.M., Tcaciuc, A.P., and Brown, G.E. (2014) Properties of impurity-bearing ferrihydrite III. Effects of Si on the structure of 2-line ferrihydrite. Geochimica et Cosmochimica Acta, 133, 168–185.

Cornell, R.M., and Schwermann, U. (2003) The iron oxides: structure, properties, reactions, occurrences and uses. 2nd ed, Wily-VCH.

815 Cudennec, Y., and Lecerf, A. (2006) The transformation of ferrihydrite into goethite or
816 hematite, revisited. Journal of Solid State Chemistry, 179, 716–722.
817 Dai, C., and Hu, Y.D. (2015) Fe(III) hydroxide nucleation and growth on Quartz in the
818 presence of Cu(II), Pb(II), and Cr(III): metal hydrolysis and adsorption. Environmental
819 Science & Technology, 49, 292-300.
820 Das, S., Hendry, M.J., and Essilfie-Dughan, J. (2011a) Effects of Adsorbed Arsenate on the
821 Rate of Transformation of 2-Line Ferrihydrite at pH 10. Environmental Science &
822 Technology, 45, 5557–5563.
823 Das, S., Hendry, M.J., and Essilfie-Dughan, J. (2011b) Transformation of Two-Line
824 Ferrihydrite to Goethite and Hematite as a Function of pH and Temperature.
825 Environmental Science & Technology, 45, 268–275.
826 Demianets, L.N., Pouchko, S.V., and Gaynutdinov, R.V. (2003) Fe_2O_3 single crystals:
827 hydrothermal growth, crystal chemistry and growth morphology. Journal of Crystal
828 Growth, 259, 165–178.
829 Dey, A., Bomans, P.H.H, Műller, F.A., Will, J., Frederik, P.M., De With, G., and Sommerdijk,
830 N.A.J.M. (2010) The role of prenucleation clusters in surface-induced calcium
831 phosphate crystallization. Nature Materials, 9, 1010-1014.
832 De Yoreo, J.J., Gilbert, P.U.P.A., Sommerdijk, N.A.J.M., Penn, R.L., Whitelam, S., Joester,
833 D., Zhang, H., Rimer, J.D., Navrotsky, A., Banfield, J.F., and others. (2015)
834 Crystallization by particle attachment in synthetic, biogenic, and geologic environments.
835 Science, 349, aaa6760.
836 Duan, X.C., Mei, L., Ma, J.M., Li, Q.H., Wang, T.H., and Zheng, W.J. (2012) Facet-induced
837 formation of hematite mesocrystals with improved lithium storage properties. Chemical
838 Communications, 48, 12204.
839 Fu, H.Y., Gao, X., Zhang, X., and Ling, L. (2022) Recent Advances in Nonclassical

Crystallization: Fundamentals, Applications, and Challenges. Crystal Growth & Design, 22, 1476–1499.

Gebauer, D., Kellermeier, M., Gale, J.D., Bergström, L., and Cölfen, H. (2014) Pre-nucleation clusters as solute precursors in crystallization. Chemical Society Reviews, 43, 2348–2371.

Gilbert, P.U.P.A., Porter, S.M., Sun, C.Y., Xiao, S., Gibson, B.M., Shenkar, N., and Knoll, A.H. (2019) Biomineralization by particle attachment in early animals. Proceedings of the National Academy of Sciences of the United States of American, 116, 17659–17665.

Gualtieri, A.F. (2000) Accuracy of XRPD QPA using the combined Rietveld-RIR method. Journal of Applied Crystallography, 33, 267-278.

Guo, H.B., and Barnard, A.S. (2011) Thermodynamic modeling of nanomorphologies of hematite and goethite. Journal of Materials Chemistry, 21, 11566.

Habraken, W.J.E.M., Tao, J., Brylka, L.J., Friedrich, H., Bertinetti, L., Schenk, A.S., Verch, A., Dmitrovic, V., Bomans, P.H.H., Frederik, P.M., and others. (2013) Ion-association complexes unite classical and non-classical theories for the biomimetic nucleation of calcium phosphate. Nature Communications, 4, 1507.

Hansel, C.M., Benner, S.G., and Fendorf, S. (2005) Competing Fe(II)-induced mineralization pathways of ferrihydrite. Environmental Science & Technology, 39, 7147-7153.

Hoashi, M., Bevacqua, D.C., Otake, T., Watanabe, Y., Hickman, A.H., Utsunomiya, S., and Ohmoto, H. (2009) Primary haematite formation in an oxygenated sea 3.46 billion years ago. Nature Geoscience, 2, 301-306.

Hochella, M.F.Jr., Kasama, T., Putnis, A., Putnis, C.V., and Moore, J.N. (2005) Environmentally important, poorly crystalline Fe/Mn hydrous oxides: ferrihydrite and a possibly new vernadite-like mineral from the Clark Fork River Superfund Complex. American Mineralogist, 90, 718-724.

865 Hochella, M. F.Jr., Lower, S.K., Maurice, P.A., Penn, R.L., Sahai, N., Sparks, D.L., and
866 Twining, B.S. (2008) Nanominerals, mineral nanoparticles, and Earth systems. Science,
867 319, 1631.
868 Hochella, M. F.Jr., Mogk, D.W., Ranville, J., Allen, I.C., Luther, G.W., Marr, L.C., McGrail,
869 B.P., Murayama, M., Qafoku, N.P., Rosso, K.M., and others. (2019) Natural, incidental,
870 and engineered nanomaterials and their impacts on the Earth system. Science, 363, 1414.
871 Hu, Y.D., Neil, C., Lee, B., and Jun, Y.S. (2013) Control of Heterogeneous Fe(III)
872 (Hydr)oxide Nucleation and Growth by Interfacial Energies and Local Saturations.
873 Environmental Science & Technology, 47, 9198–9206.
874 Huang, M.L., Yan, Y., Feng, W.H., Weng, S.X., Zheng, Z.Y., Fu, X.Z., and Liu, P. (2014)
875 Controllable Tuning Various Ratios of ZnO Polar Facets by Crystal Seed-Assisted
876 Growth and Their Photocatalytic Activity. Crystal Growth & Design, 14, 2179–2186.
877 Huang, X.P., Hou, X.J., Song, F.H., Zhao, J.C., and Zhang, L.Z. (2016) Facet-dependant
878 Cr(VI) adsorption of hematite nanocrystals. Environmental Science & Technology, 50,
879 1964-1972.
880 Huang, M.Y., Liu, C., Cui, P.X., Dang, F., Zhou, J., Liu, M.L., and Wang, Y.J. (2023) Facet-
881 specific cation exchange and heterogeneous transformation of cadmium sulfide
882 nanoparticles induced by Cu(II). Environmental Science: Nano, 10, 463-475.
883 Hyland, E.G., Sheldon, N.D., Van der Voo, R., Badgley, C., and Abrajevitch, A. (2015) A new
884 paleoprecipitation proxy based on soil magnetic properties: Implications for expanding
885 paleoclimate reconstructions. Geological Society of America Bulletin, B31207.1.
886 Jehannin, M., Rao, A., and Cölfen, H. (2019) New horizons of nonclassical crystallization.
887 Journal of the American Chemical Society, 141, 10120-10136.
888 Jiang, Y., Kellermeier, M., Gebauer, D., Lu, Z., Rosenberg, R., Moise, A., Przybylski, M., and
889 Cölfen, H. (2018a) Growth of organic crystals via attachment and transformation of

890 nanoscopic precursors. Nature Communications, 8, 15933.

891 Jiang, Z.X., Liu, Q.S., Roberts, A.P., Barrón, V., Torrent, J., and Zhang, Q. (2018b) A new
892 model for transformation of ferrihydrite to hematite in soils and sediments. Geology, 46,
893 987-990.

894 Jun, Y.S., Lee, B., and Waychunas, G.A. (2010) In situ observations of nanoparticles early
895 development kinetics at mineral-water interfaces. Environmental Science & Technology,
896 44, 8182-8189.

897 Jun, Y.S., Kim, D., and Neil, C.W. (2016) Heterogeneous nucleation and growth of
898 nanoparticles at environmental interfaces. Accounts of Chemical Research, 49, 1681-
899 1690.

900 Jun, Y.S., Zhu, Y.G., Wang, Y., Ghim, D., Wu, X.H., Kim, D., and Jung, H. (2022) Classical
901 and Nonclassical Nucleation and Growth Mechanisms for Nanoparticle Formation.
902 Annual Review of Physical Chemistry, 73, 453–477.

903 Jung, H., and Jun, Y.S. (2016) Ionic Strength-Controlled Mn (Hydr)oxide Nanoparticle
904 Nucleation on Quartz: Effect of Aqueous $Mn(OH)_2$. Environmental Science &
905 Technology, 50, 105–113.

906 Jung, H., Lee, B., and Jun, Y.S. (2016) Structural Match of Heterogeneously Nucleated
907 $Mn(OH)_2(s)$ Nanoparticles on Quartz under Various pH Conditions. Langmuir, 32,
908 10735–10743.

909 Kappler, A., Bryce, C., Mansor, M., Lueder, U., Byrne, J.M., and Swanner, E.D. (2021) An
910 evolving view on biogeochemical cycling of iron. Nature Reviews Microbiology, 19,
911 360–374.

912 Khaleghi, A., Sadrameli, S.M., and Manteghi, M. (2020) Thermodynamic and kinetics
913 investigation of homogeneous and heterogeneous nucleation. Reviews in Inorganic
914 Chemistry, 40, 167-192.

915 Kulmala, M. (2003) How Particles Nucleate and Grow. Science, 302, 1000–1001.

916 Lewis, D.G. (1992) Transformation induced in ferrihydrite by oven-drying. Zeitschrift fur
917 Pflanzenernährung und Bodenkunde, 155, 461-466.

918 Li, J.J., and Deepak, F.L. (2022) *In Situ* Kinetic Observations on Crystal Nucleation and
919 Growth. Chemical Reviews, 122, 16911–16982.

920 Li, Q., Fernandez-Martinez, A., Lee, B., Waychunas, G.A., and Jun, Y.S. (2014) Interfacial
921 Energies for Heterogeneous Nucleation of Calcium Carbonate on Mica and Quartz.
922 Environmental Science & Technology, 48, 5745–5753.

923 Lin, H.X., Lei, Z.C., Jiang, Z.Y., Hou, C.P., Liu, D.Y., Xu, M.M., Tian, Z.Q., and Xie, Z.X.
924 (2013) Supersaturation-Dependent Surface Structure Evolution: From Ionic, Molecular
925 to Metallic Micro/Nanocrystals. Journal of American Chemical Society, 135, 9311–9314.

926 Lin, X.M., Burns, R.C., and Lawrance, G.A. (2003) Effect of cadmium(II) and anion type on
927 the ageing of ferrihydrite and its subsequent leaching under neutral and alkaline
928 conditions. Water Air and Soil pollution, 143, 155-177.

929 Liu, J., Inoué, S., Zhu, R.L., He, H.P., and Hochella, M.F.Jr. (2021a) Facet-specific oxidation
930 of Mn(II) and heterogeneous growth of manganese (oxyhydr)oxides on hematite
931 nanoparticles. Geochimica et Cosmochimica Acta, 307, 151–167.

932 Liu, J., Zhu, R.L., Ma, L.Y., Fu, H.Y., Lin, X.J., Parker, S.C., and Molinari, M. (2021b)
933 Adsorption of phosphate and cadmium on iron (oxyhydr)oxides: A comparative study on
934 ferrihydrite, goethite, and hematite. Geoderma, 383, 114799.

935 Liu, J, Sheng, A.X., Li, X.X., Arai, Y., Ding, Y.F., Nie, M.J., Yan, M.Q., and Rosso, K.M.
936 (2022a) Understanding the Importance of Labile Fe(III) during Fe(II)-Catalyzed
937 Transformation of Metastable Iron Oxyhydroxides. Environmental Science &
938 Technology, 56, 3801–3811.

939 Liu, J, Chen, Q.Z., Yang, Y.X., Wei, H.Y., Laipan, M.W., Zhu, R.L., He, H.P., and Hochella,

M.F.Jr. (2022b) Coupled redox cycling of Fe and Mn in the environment: The complex interplay of solution species with Fe- and Mn-(oxyhydr)oxide crystallization and transformation. Earth-Science Reviews, 232, 104105.

Loan, M., Parkinson, G.M., and Richmond, W.R. (2005) The effect of zinc sulfide on phase transformation of ferrihydrite. American Mineralogist, 90, 258-261.

Michel, F.M., Ehm, L., Antao, S.M., Lee, P.L., Chupas, P.J., Liu, G., Strongin, D.R., Schoonen, M.A.A., Phillips, B.L., and Parise, J.B. (2007) The Structure of Ferrihydrite, a Nanocrystalline Material. Science, 316, 1726–1729.

Molnár, Z., Dódony, I., and Pósfai, M. (2023) Transformation of amorphous calcium carbonate in the presence of magnesium, phosphate, and mineral surfaces. Geochimica et Cosmochimica Acta, 345, 90–101.

Murad, E. (1996) Magnetic properties of microcrystalline iron (III) oxides and related materials as reflected in their Mössbauer spectra. Physics and Chemistry Minerals, 23, 248–262.

Namayandeh, A., Borkiewicz, O.J., Bompoti, N.M., Chrysochoou, M., and Michel, F.M. (2022) Oxyanion Surface Complexes Control the Kinetics and Pathway of Ferrihydrite Transformation to Goethite and Hematite. Environmental Science & Technology, 56, 15672–15684.

Nguyen, D.T., Park, D.W., and Kim, K.S. (2011) Seed-Mediated Synthesis of Iron Oxide and Gold/Iron Oxide Nanoparticles. Journal of Nanoscience and Nanotechnology, 11, 7214–7217.

Notini, L., ThomasArrigo, L.K., Kaegi, R., and Kretzschmar, R. (2022) Coexisting Goethite Promotes Fe(II)-Catalyzed Transformation of Ferrihydrite to Goethite. Environmental Science & Technology, 56, 12723–12733.

Nudelman, F., Pieterse, K., George, A., Bomans, P.H.H., Friedrich, H., Brylka, L.J., Hilbers,

965 P.A.J., de With, G., and Sommerdijk, N.A.J.M. (2010) The role of collagen in bone
966 apatite formation in the presence of hydroxyapatite nucleation inhibitors. Nature
967 Materials, 9, 1004–1009.
968 Ouyang, J.J., Pei, J., Kuang, Q., Xie, Z.X., and Zheng, L.S. (2014) Supersaturation-
969 Controlled Shape Evolution of α-Fe_2O_3 Nanocrystals and Their Facet-Dependent
970 Catalytic and Sensing Properties. ACS Applied Materials & Interfaces, 6, 12505–12514.
971 Politi, Y., Metzler, R.A., Abrecht, M., Gilbert, B., Wilt, F.H., Sagi, I., Addadi, L., Weiner, S.,
972 and Gilbert, U.P.A. (2008) Transformation mechanism of amorphous calcium carbonate
973 into calcite in the sea urchin larval spicule. Proceedings of the National Academy of
974 Sciences of the United States of American, 105, 17362-17366.
975 Prywer, J. (2004) Explanation of some peculiarities of crystal morphology deduced from the
976 BFDH law. Journal of Crystal Growth, 270, 699–710.
977 Putnis, A. (2014) Why Mineral Interfaces Matter. Science, 343, 1441–1442.
978 Riechers, S.L., Rosso, K.M., and Kerisit, S.N. (2017) Nucleation and Epitaxy-Mediated
979 Phase Transformation of a Precursor Cadmium Carbonate Phase at the Calcite/Water
980 Interface. Journal of Physical Chemistry C, 121, 5012–5019.
981 Riechers, S.L., Ilton, E.S., Qafoku, O., Du, Y., and Kerisit, S.N. (2022) Cobalt hydroxide–
982 cobalt carbonate competitive growth on carbonate surfaces. Chemical Geology, 605,
983 120951.
984 Rodriguez-Navarro, C., Burgos Cara, A., Elert, K., Putnis, C.V., and Ruiz-Agudo, E. (2016)
985 Direct nanoscale imaging reveals the growth of calcite crystals via amorphous
986 nanoparticles. Crystal Growth & Design, 16, 1850-1860.
987 Rosso, K.M., Yanina, S.V., Gorski, C.A., Larese-Casanova, P., and Scherer, M.M. (2010)
988 Connecting Observations of Hematite (α-Fe_2O_3) Growth Catalyzed by Fe(II).
989 Environmental Science & Technology, 44, 61–67.

990 Sakakibara, M., Tanaka, M., Takahashi, Y., and Murakami, T. (2019) Redistribution of Zn
991 during transformation of ferrihydrite: Effects of initial Zn concentration. Chemical
992 Geology, 522, 121–134.
993 Schwertmann, U., and Murad, E. (1983) Effect of pH on the Formation of Goethite and
994 Hematite from Ferrihydrite. Clays and Clay Minerals, 31, 277–284.
995 Shaw, S. (2005) The kinetics and mechanisms of goethite and hematite crystallization under
996 alkaline conditions, and in the presence of phosphate. American Mineralogist, 90, 1852–
997 1860.
998 Sheng, A.X., Liu, J., Li, X.X., Luo, L.L., Ding, Y.F., Chen, C.M., Zhang, X., Wang, C.M., and
999 Rosso, K.M. (2021) Labile Fe(III) supersaturation controls nucleation and properties of
1000 product phases from Fe(II)-catalyzed ferrihydrite transformation. Geochimica et
1001 Cosmochimica Acta, 309, 272–285.
1002 Silva, L.S., Marques Júnior, J., Barrón, V., Gomes, R.P., Teixeira, D.D.B., Siqueira, D.S., and
1003 Vasconcelos, V. (2020) Spatial variability of iron oxides in soils from Brazilian
1004 sandstone and basalt. Catena, 185, 104258.
1005 Solits, J.A., Feinberg, J.M., Gilber, B., and Penn, R.L. (2016) Phase transformation and
1006 particle-mediated growth in the formation of hematite from 2-line ferrihydrite. Crystal
1007 Growth & Design, 16, 922-932.
1008 Stirner, T., Scholz, D., and Sun, J. (2020) Convergence of surface energy calculations for
1009 various methods: (001), (012), (100) hematite and the applicability of the standard
1010 approach. Journal of Physics: Condensed Matter, 32, 185002.
1011 Thanh, N.T.K., Maclean, N., and Mahiddine, S. (2014) Mechanisms of Nucleation and
1012 Growth of Nanoparticles in Solution. Chemical Reviews, 114, 7610–7630.
1013 ThomasArrigo, L.K., Bouchet, S., Kaegi, R., and Kretzschmar, R. (2020) Organic matter
1014 influences transformation products of ferrihydrite exposed to sulfide. Environmental

Science: Nano, 7, 3405-3418.

Voelz, J.L., Arnold, W.A., and Penn, R.L. (2018) Redox-induced nucleation and growth of goethite on synthetic hematite nanoparticles. American Mineralogist, 103, 1021–1029.

Wei, H.Y., Liu, J., Chen, Q.Z., Zhu, R.L., Yan, L.X., Yang, Y.X., Liang, X.L., Zhu, J.X., and He, H.P. (2023) Heterogeneous and retarded phase transformation of ferrihydrite on montmorillonite surface: The important role of surface interactions. American Mineralogist, 108, 865–880.

Wu, F., Hua, J., Zhou, J.M., Liu, Y.H., Long, S.Q., Fei, Y.H., and Liu, C.S. (2021) Facet-specific reactivity of hematite nanocrystals during Fe(II)-catalyzed recrystallization. Chemical Geology, 583, 120460.

Wu, H., Yang, T., Du, Y.H., Shen, L., and Ho, G.W. (2018) Identification of Facet-Governing Reactivity in Hematite for Oxygen Evolution. Advanced Materials, 30, 1804341.

Wu, J.H., Shi, M.Q., Feng, F., Hao, J.T., Zhao, D., Wang, X.Y., Li, J.W., Zhang, W.C., Wang, Q.W., Ke, Y., and others. (2023) Recent advances in magnetite crystallization: pathway, modulation, and characterization. Crystal Growth & Design, 23, 6201-6218.

Wu, X.H., Lee, B., and Jun, Y.S. (2020) Interfacial and activation energies of environmentally abundant heterogeneously nucleated iron(III) (hydr)oxide in quartz. Environmental Science & Technology, 54, 12119-12129.

Xu, M., Kovarik, L., Arey, B.W., Felmy, A.R., Rosso, K.M., and Kerisit, S. (2014a) Kinetics and mechanisms of cadmium carbonate heteroepitaxial growth at the calcite ($10\bar{1}4$) surface. Geochimica et Cosmochimica Acta, 134, 221–233.

Xu, M., Ilton, E.S., Engelhard, M.H., Qafoku, O., Felmy, A.R., Rosso, K.M., and Kerisit, S. (2014b) Heterogeneous growth of cadmium and cobalt carbonate phases at the (10-14) calcite surface. Chemical Geology, 397, 24-36.

Yan, L.X., Zhu, R.L., Liu, J., Yang, Y.X., Zhu, J.X., Sun, H.J., and He, H.P. (2020) Effects of

Fullerol and Graphene Oxide on the Phase Transformation of Two-Line Ferrihydrite. ACS Earth Space Chemistry, 4, 335–344.

Yan, L.X., Chen, Q.Z., Yang, Y.X., and Zhu, R.L. (2021) The significant role of montmorillonite on the formation of hematite nanoparticles from ferrihydrite under heat treatment. Applied Clay Science, 202, 105962.

Yanina, S.V., and Rosso, K.M. (2008) Linked Reactivity at Mineral-Water Interfaces Through Bulk Crystal Conduction. Science, 320, 218–222.

Yang, Y.X, Liu, J., Zhu, R.L, Chen, Q.Z, Wei, H.Y, Chen, M., Xian, H.Y., and He, H.P. (2023) surface-induced oxidation of Mn(II) and crystallization of manganese (hydr)oxides on clay minerals. Geochimica et Cosmochimica Acta, 363, 129-146.

Ye, C.J., Ariya, P.A., Fu, F.L., Yu, G.D., and Tang, B. (2021) Influence of Al(III) and Sb(V) on the transformation of ferrihydrite nanoparticles: Interaction among ferrihydrite, coprecipitated Al(III) and Sb(V). Journal of Hazardous Materials, 408, 124423.

Yee, N., Shaw, S., Benning, L.G., and Nguyen, T.H. (2006) The rate of ferrihydrite transformation to goethite via the Fe(II) pathway. American Mineralogist, 91, 92-96.

Yuan, Q.L., Li, P.F., Liu, J., Lin, Y., Cai, Y.Y., Ye, Y.X., and Liang, C.H. (2017) Facet-Dependent Selective Adsorption of Mn-Doped α-Fe_2O_3 Nanocrystals toward Heavy-Metal Ions. Chemistry of Materials, 29, 10198–10205.

Yuwono, V.M., Burrows, N.D., Soltis, J.A., and Penn, R.L. (2010) Oriented Aggregation: Formation and Transformation of Mesocrystal Intermediates Revealed. Journal of the American Chemical Society, 132, 2163–2165.

Zhang, D.N., Wang, S.F., Wang, Y., Gomez, M.A., Duan, Y.H., and Jia, Y.F. (2018) The Transformation of Two-Line Ferrihydrite into Crystalline Products: Effect of pH and Media (Sulfate versus Nitrate). ACS Earth and Space Chemistry, 2, 577–587.

Zhao, L.L., Hong, H.L., Fang, Q., Yin, K., Wang, C.W., Li, Z.H., Torrent, J., Cheng, F., and

Algeo, T.J. (2017) Monsoonal climate evolution in southern China since 1.2 Ma: New constraints from Fe-oxide records in red earth sediments from the Shengli section, Chengdu Basin. Palaeogeography Palaeoclimatology Palaeoecology, 473, 1–15.

Zhu, G.M., Sushko, M.L., Loring, J.S., Legg, B.A., Song, M., Soltis, J.A., Huang, X., Rosso, K.M., and De Yoreo, J.J. (2021) Self-similar mesocrystals form via interface-driven nucleation and assembly. Nature, 590, 416–422.

Zhu, M.Q., Frandsen, C., Wallace, A.F., Legg, B., Khalid, S., Zhang, H.Z., Morup, S., Banfield, J.F., and Waychunas, G.A. (2016) Precipitation pathways for ferrihydrite formation in acidic solutions. Geochimica et Cosmochimica Acta, 172, 247-264.

FIGURE CAPTIONS

Figure 1. XRD patterns recording the transformation process of pure Fhy at **(a)** pH 4, **(b)** pH 7, and **(c)** pH 12; XRD patterns recording the transformation process of Fhy-20Hem at **(d)** pH 4, **(e)** pH 7, and **(f)** pH 12.

Figure 2. The Mössbauer spectra of **(a)** Fhy-4-10d, **(b)** Fhy-7-10d, **(c)** Fhy-12-24h, **(d)** Fhy-20Hem-4-10d, **(e)** Fhy-20Hem-7-10d, and **(f)** Fhy-20Hem-12-24h. Red area: Fhy, blue area: Hem, orange area: Gth. The fitting parameters and relative contents were listed at the bottom of their pictures.

Figure 3. The residual Fhy contents (calculated using ammonium oxalate dissolution method) in pure Fhy and Fhy-20Hem samples after transformation for different times at **(a)** pH 4, **(b)** pH 7, and **(c)** pH 12.

Figure 4. **(a)** The XRD patterns of the samples with different content of Hem nanoplates after reacting 10 days at pH 4; **(b)** the theoretical and actual contents of Hem in these reacted samples (left vertical axis), and the residual Fhy content after reacting at pH 4 for 3 days in different samples (right vertical axis).

Figure 5. SEM images of **(a)** Fhy-4-10d, **(b)** Fhy-20Hem-4-10d, **(c)** Fhy-7-10d, **(d)** Fhy-20Hem-7-10d, **(e)** Fhy-12-24h, and **(f)** Fhy-20Hem-12-24h.

Figure 6. **(a)** The shape model of the Hem nanoplates evolution with time in different directions; **(b)** SEM images of Fhy-20Hem after reacting for different times at pH 4; **(c)** the shape characteristics of the side facet of Hem nanoplates after reacted, which is consistent with the combination of {113}, {012}, and {001} facets; **(d)** TEM image of the Hem nanoplates before reacted, and the inset represents the histogram of the size distribution for the width of hexagonal Hem; **(e)** TEM image of the Fhy-20Hem-4-3d, and the inset represents the histogram of the size distribution for the width of the reacted Hem nanoplates; **(f)** TEM image of Fhy-20Hem-4-10d; **(g-h)** the HRTEM of the corresponding area in **g**, and the insets in **g** and **h** represent the corresponding FFT patterns.

Figure 7. **(a)** TEM image of the flower-like iron oxides in the Fhy-20Hem-12-24h sample; **(b and d)** HRTEM image of the corresponding area in **a**; **(c)** the FFT pattern of **b**; **(e and f)** the FFT patterns of the corresponding areas in **d**. These FFT results demonstrated that the petals of the flower-like iron oxides are Gth along the [$\bar{2}$00] zone axis, and the center of the flower-like iron oxides is Hem along the [001] zone axis. **(g)** Top view (from the perspective of Hem [001] and Gth [$\bar{2}$00]) of the atomic structure of Hem and Gth crystals, and the spatial positions of oxygen and iron in Hem and Gth match very well from the presented perspective. **(h)** The side view (from the perspective of Hem [$\bar{1}$10] and Gth [0$\bar{1}$2]) of the atomic structure of Hem and Gth.

Figure 8. **(a)** The relative contents of Hem and Gth in different systems. Fhy-Hem: the samples represent the actual contents of Hem and Gth with the effect of Hem nanoplates; Fhy+Hem: the samples represent the theoretical contents of Hem and Gth assuming that the added Hem does not affect the transformation of Fhy. **(b)** The flowchart of Fhy transformation in the presence of Hem nanoplates under different conditions. Induced Hem

1116 represents the difference between the actual Hem content in Fhy-Mnt and theoretical Hem
1117 content in Fhy+Hem. It needs to be stated that the induced Hem content in the sample with
1118 70 wt% Hem nanoplates is far larger than 21.4 wt% due to the excess Hem nanoplates
1119 causing the complete transformation of Fhy to Hem. **(c)** The transformation process of Fhy in
1120 the presence of Hem nanoplates through different pathways and the induced growth mode of
1121 Hem nanoplates during the transformation of Fhy.

Figure 1

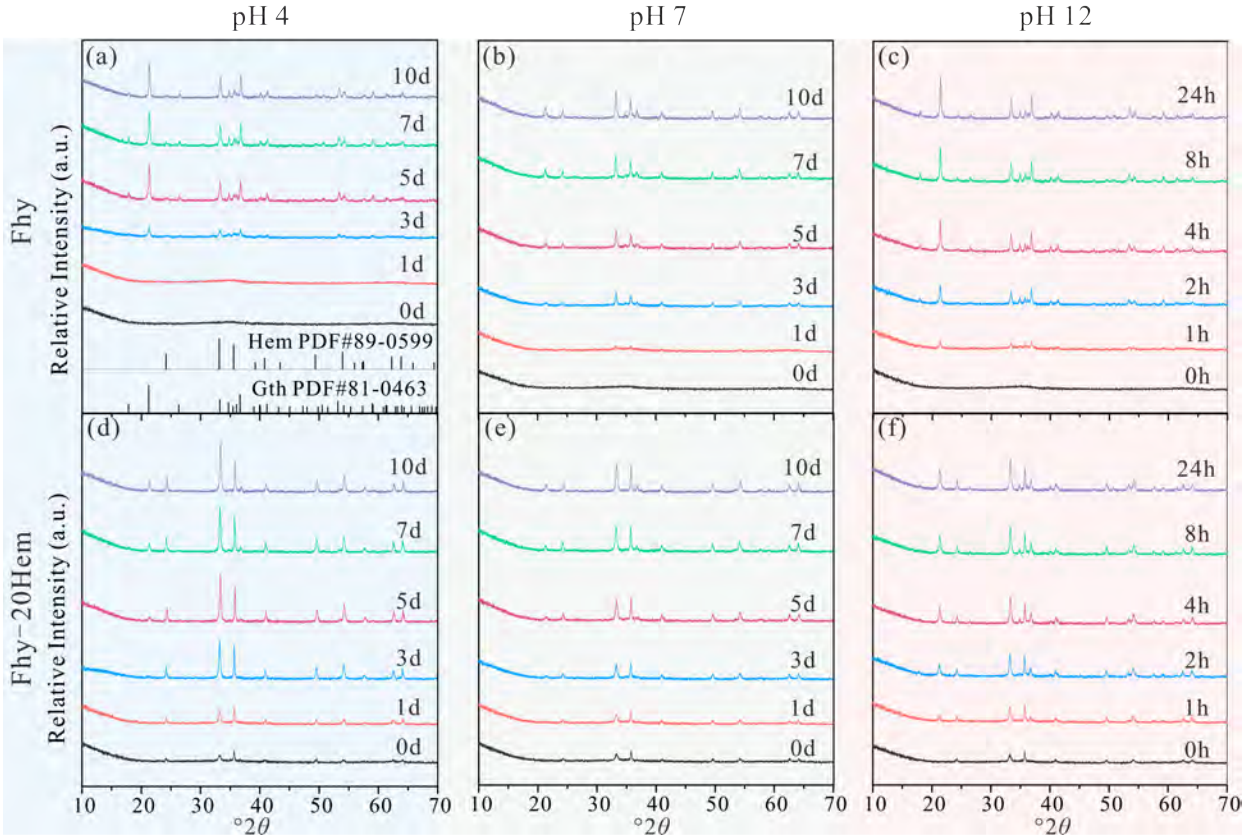
pH 4
pH 7
pH 12
Fhy
Fhy−20Hem
Relative Intensity (a.u.)
(a)
(b)
(c)
(d)
(e)
(f)
10d
7d
5d
3d
1d
0d
24h
8h
4h
2h
1h
0h
Hem PDF#89-0599
Gth PDF#81-0463
10 20 30 40 50 60 70
°2θ

Figure 2

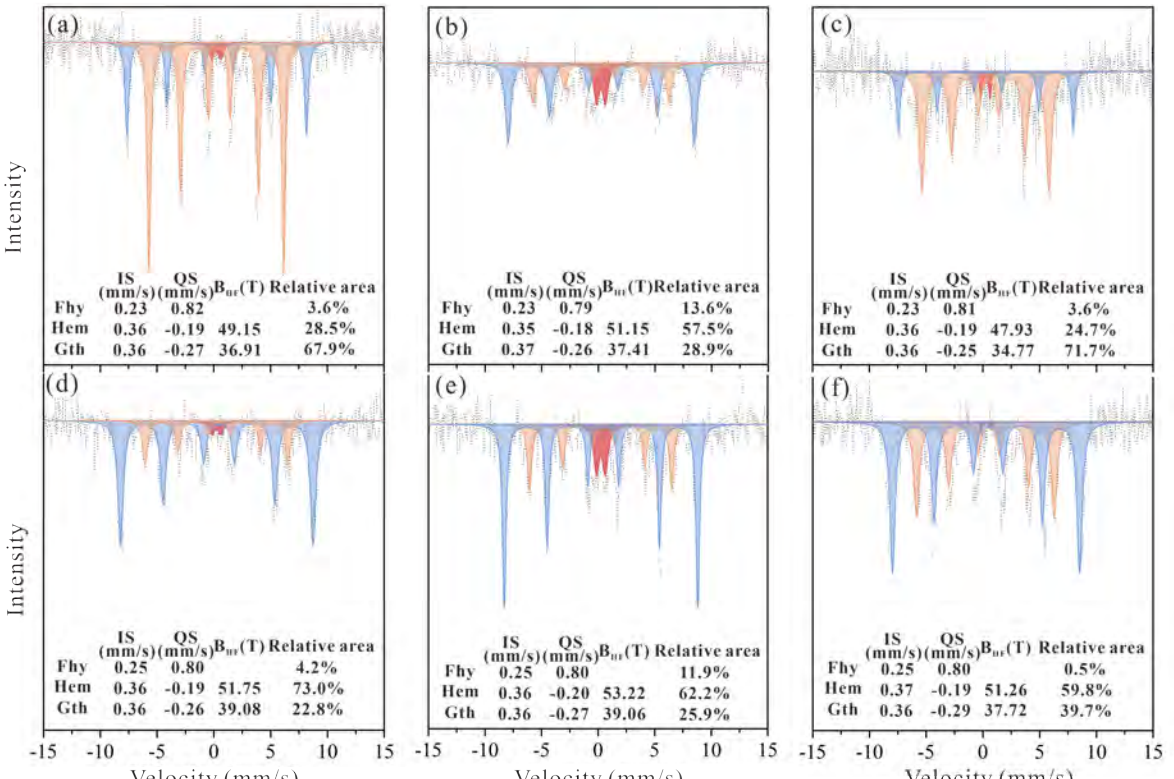
(a)
IS (mm/s) QS (mm/s) B_{hf}(T) Relative area
Fhy 0.23 0.82 3.6%
Hem 0.36 -0.19 49.15 28.5%
Gth 0.36 -0.27 36.91 67.9%
(b)
IS (mm/s) QS (mm/s) B_{hf}(T) Relative area
Fhy 0.23 0.79 13.6%
Hem 0.35 -0.18 51.15 57.5%
Gth 0.37 -0.26 37.41 28.9%
(c)
IS (mm/s) QS (mm/s) B_{hf}(T) Relative area
Fhy 0.23 0.81 3.6%
Hem 0.36 -0.19 47.93 24.7%
Gth 0.36 -0.25 34.77 71.7%
(d)
IS (mm/s) QS (mm/s) B_{hf}(T) Relative area
Fhy 0.25 0.80 4.2%
Hem 0.36 -0.19 51.75 73.0%
Gth 0.36 -0.26 39.08 22.8%
(e)
IS (mm/s) QS (mm/s) B_{hf}(T) Relative area
Fhy 0.25 0.80 11.9%
Hem 0.36 -0.20 53.22 62.2%
Gth 0.36 -0.27 39.06 25.9%
(f)
IS (mm/s) QS (mm/s) B_{hf}(T) Relative area
Fhy 0.25 0.80 0.5%
Hem 0.37 -0.19 51.26 59.8%
Gth 0.36 -0.29 37.72 39.7%
Intensity
Intensity
-15 -10 -5 0 5 10 15
Velocity (mm/s)
Velocity (mm/s)
Velocity (mm/s)

Figure 3

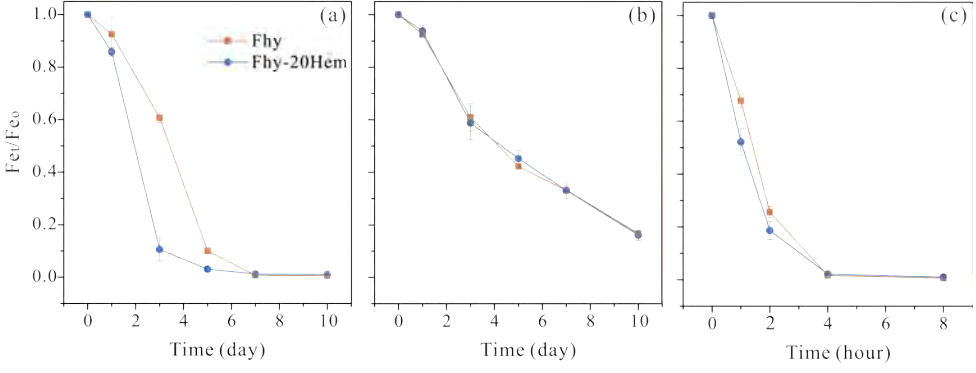
(a)
(b)
(c)
Fhy
Fhy-20Hem
Fe₀/Fe₀
1.0
0.8
0.6
0.4
0.2
0.0
0
2
4
6
8
10
Time (day)
Time (day)
Time (hour)

Figure 4

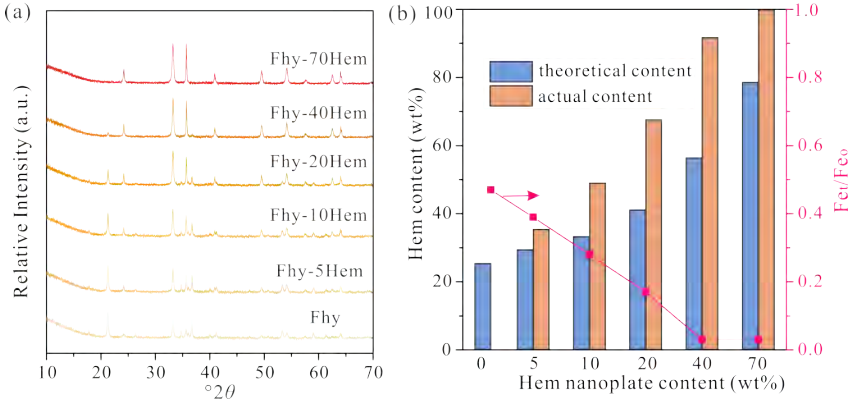
(a)
Relative Intensity (a.u.)
Fhy-70Hem
Fhy-40Hem
Fhy-20Hem
Fhy-10Hem
Fhy-5Hem
Fhy
10
20
30
40
50
60
70
°2θ
(b)
Hem content (wt%)
theoretical content
actual content
Fet/Fe0
0
20
40
60
80
100
0.0
0.2
0.4
0.6
0.8
1.0
0
5
10
20
40
70
Hem nanoplate content (wt%)

Figure 5

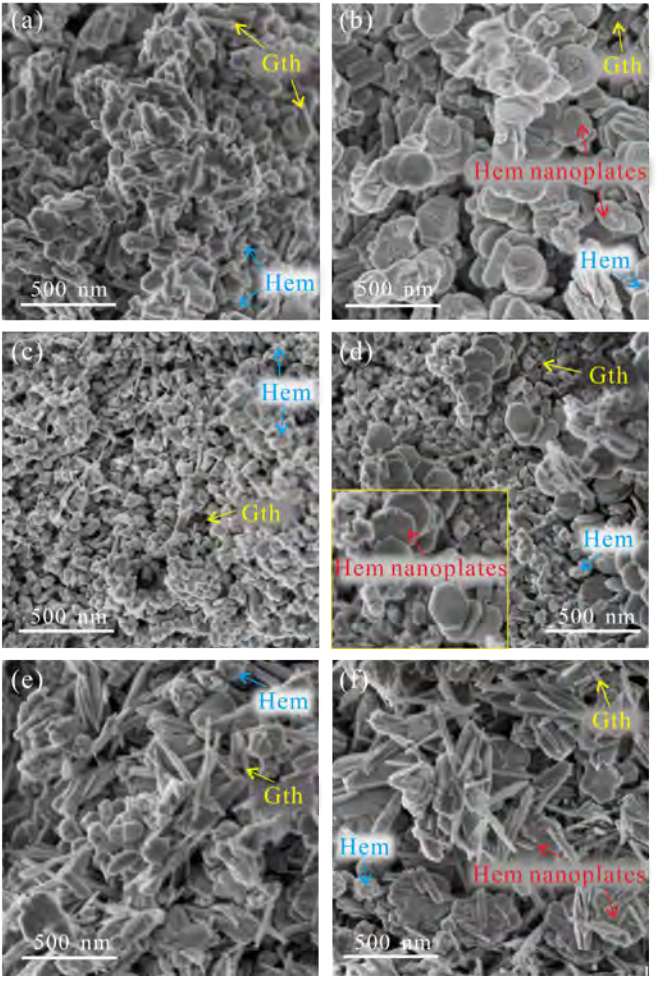
(a)
Gth
Hem
500 nm
(b)
Gth
Hem nanoplates
Hem
500 nm
(c)
Hem
Gth
500 nm
(d)
Gth
Hem nanoplates
Hem
500 nm
(e)
Hem
Gth
500 nm
(f)
Gth
Hem
Hem nanoplates
500 nm

Figure 6

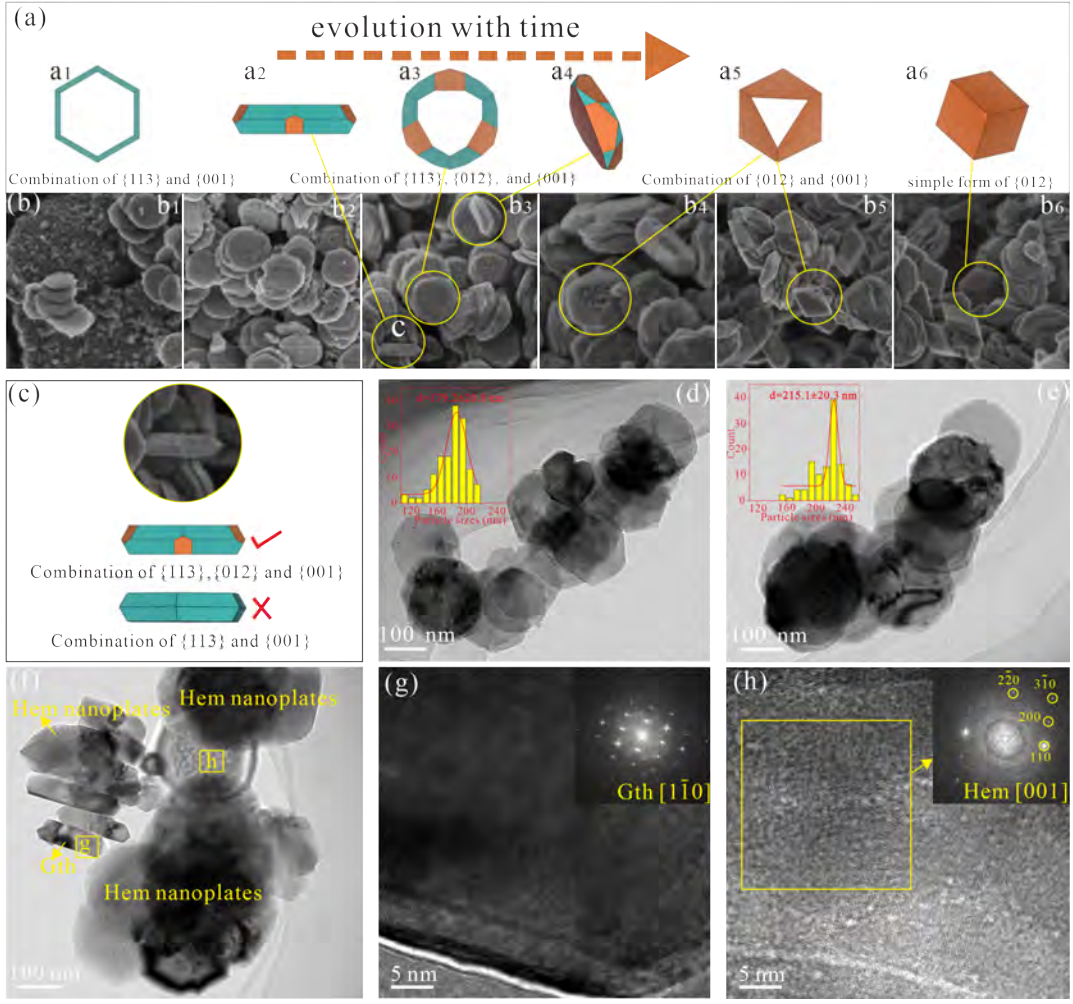
(a)
evolution with time
a1
a2
a3
a4
a5
a6
Combination of {113} and {001}
Combination of {113}, {012}, and {001}
Combination of {012} and {001}
simple form of {012}
(b)
b1
b2
b3
b4
b5
b6
c
(c)
Combination of {113}, {012} and {001}
Combination of {113} and {001}
(d)
100 nm
(e)
d=215.1±20.3 nm
Count
Particle size (nm)
100 nm
(f)
Hem nanoplates
Hem nanoplates
Hem
Gth
Hem nanoplates
100 nm
(g)
Gth [1$\bar{1}$0]
5 nm
(h)
2$\bar{2}$0
3$\bar{1}$0
200
110
Hem [001]
5 nm

Figure 7

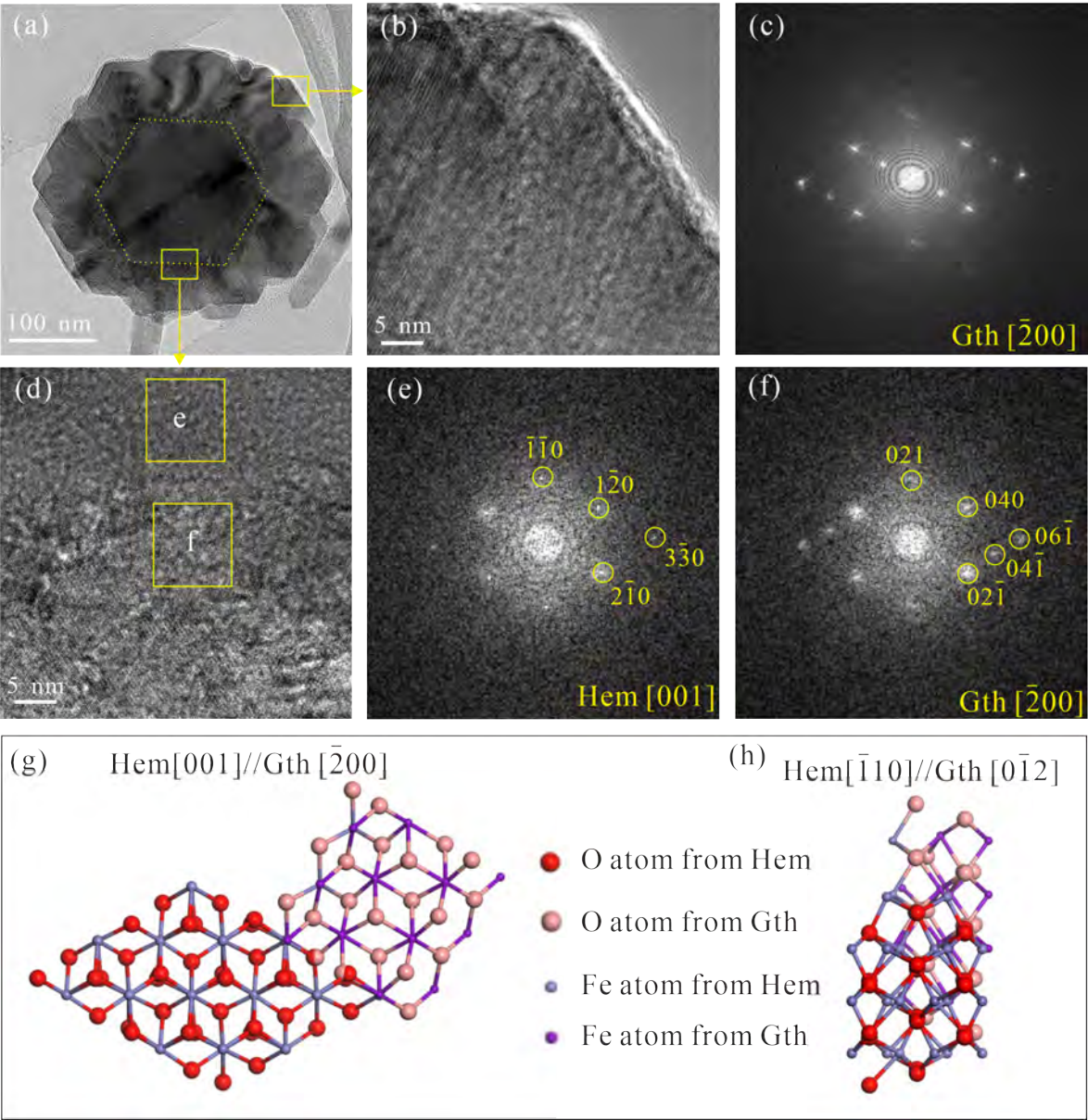
(a)
100 nm
(b)
5 nm
(c)
Gth [$\bar{2}$00]
(d)
e
f
5 nm
(e)
$\bar{1}\bar{1}$0
1$\bar{2}$0
3$\bar{3}$0
2$\bar{1}$0
Hem [001]
(f)
021
040
06$\bar{1}$
04$\bar{1}$
02$\bar{1}$
Gth [$\bar{2}$00]
(g)
Hem[001]//Gth [$\bar{2}$00]
O atom from Hem
O atom from Gth
Fe atom from Hem
Fe atom from Gth
(h)
Hem[$\bar{1}$10]//Gth [0$\bar{1}$2]

Figure 8

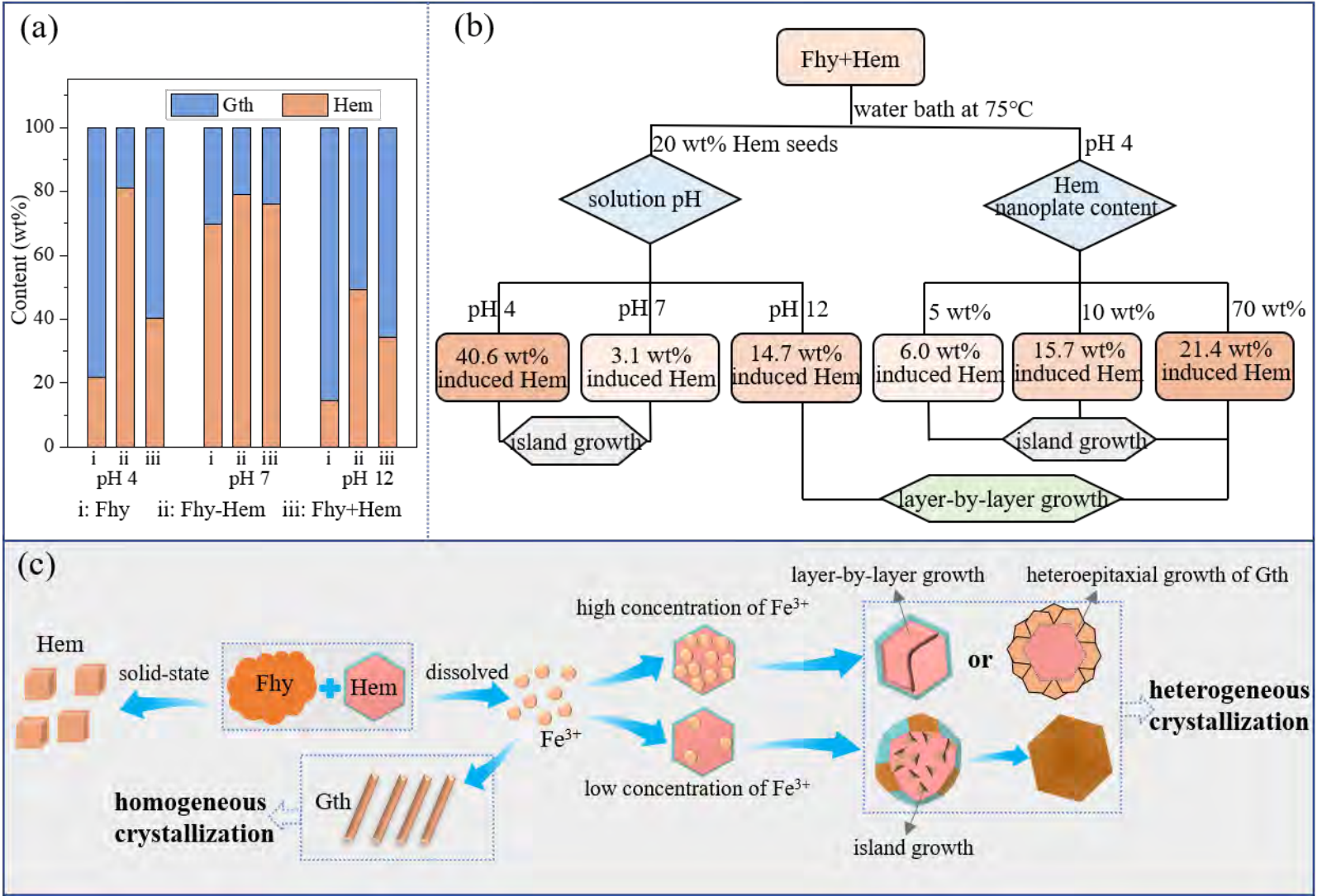
(a)
Gth
Hem
Content (wt%)
100
80
60
40
20
0
i ii iii
pH 4
i ii iii
pH 7
i ii iii
pH 12
i: Fhy
ii: Fhy-Hem
iii: Fhy+Hem
(b)
Fhy+Hem
water bath at 75°C
20 wt% Hem seeds
pH 4
solution pH
Hem nanoplate content
pH 4
pH 7
pH 12
5 wt%
10 wt%
70 wt%
40.6 wt% induced Hem
3.1 wt% induced Hem
14.7 wt% induced Hem
6.0 wt% induced Hem
15.7 wt% induced Hem
21.4 wt% induced Hem
island growth
island growth
layer-by-layer growth
(c)
Hem
solid-state
Fhy
Hem
dissolved
Fe3+
high concentration of Fe3+
low concentration of Fe3+
layer-by-layer growth
heteroepitaxial growth of Gth
or
heterogeneous crystallization
island growth
homogeneous crystallization
Gth